FH University of Applied Sciences TECHNIKUM WIEN

MASTER THESIS

Thesis submitted in partial fulfillment of the requirements for the degree of Master of Science in Engineering at the University of Applied Sciences Technikum Wien - Degree Program TW

Enhancement of a mechanical eye model setup for IOL testing

By: Bc. Ferdinand Dvořák

Student Number: 2110228010

Supervisors: FH-Prof. DI Dr. Lukas Traxler, BSc
Dipl.-Ing. Andrea Balz, BSc

Vienna, October 23, 2022

Declaration

“As author and creator of this work to hand, I confirm with my signature knowledge of the relevant copyright regulations governed by higher education acts (see Urheberrechtsgesetz /Austrian copyright law as amended as well as the Statute on Studies Act Provisions / Examination Regulations of the UAS Technikum Wien as amended).

I hereby declare that I completed the present work independently and that any ideas, whether written by others or by myself, have been fully sourced and referenced. I am aware of any consequences I may face on the part of the degree program director if there should be evidence of missing autonomy and independence or evidence of any intent to fraudulently achieve a pass mark for this work (see Statute on Studies Act Provisions / Examination Regulations of the UAS Technikum Wien as amended).

I further declare that up to this date I have not published the work to hand nor have I presented it to another examination board in the same or similar form. I affirm that the version submitted matches the version in the upload tool.“

Vienna, October 23, 2022

Signature

Ferdinand Dvořák

Digitálně podepsal Ferdinand Dvořák
Datum: 2022.10.23 23:14:11 +02'00'

Abstract

Cataract is the most common cause of blindness. The only way to treat it is the cataract surgery during which the affected crystalline lens is destroyed and removed from the eye and replaced with an implantable intraocular lens. After the cataract surgery, a displacement of the intraocular lens from its aligned position happens in some cases. The lenses may be of several designs and their properties are subject to regulatory standards. These standards, however, do not include testing of the postoperative displacement of the lens. For this purpose, an optomechanical eye model setup was previously developed to enable measuring of the wavefront aberrations of the intraocular lenses. As this setup does not perfectly mimic the physiology of the human eye and the manipulation with it may sometimes introduce unwanted errors, the objective of this thesis is to fight the above-mentioned imperfections and develop a new, enhanced eye model setup which will address these.

Keywords: human eye, eye model, cataract, intraocular lens, retina

Acknowledgements

I would like to sincerely thank both of my supervisors for their friendly approach in which they treated me and which beyond other things, motivated me throughout the process of developing my master thesis. My deepest gratitude belongs to FH-Prof. DI Dr. Lukas Traxler, BSc for the supervision of my thesis. I would like to thank him for the time he was willing to sacrifice in favour of my work on this thesis, for his patient approach and invaluable advice and deep insight. Additionally, many thanks go to Dipl.-Ing. Andrea Balz, BSc for her supervision of my thesis, valuable comments on its structure, guidance throughout this process with a friendly approach and assisting in general when it was needed. I am very grateful for having the opportunity of this enriching experience of studying at the FH Technikum Wien as an exchange Double Degree student. This gratitude also relates to the chance of working on my master thesis within the warm atmosphere of the FH Technikum grounds, and to the financial support of this research. I also want to thank the laboratory assistants for their help, mainly with the 3D printing. Last but not least, I show huge gratitude to my family for supporting me in each and every aspect of the entire journey in my studies.

Contents

1 Introduction

Vision provides human brain with the highest amount of information [24] making it our dominant sense. Having a decent and healthy state of our sight is therefore critical and one should not take this for granted. Sight can be affected by many diseases or visual impairments. Some of these may be congenital, others develop in the course of lifetime. Cataract, being (in most of the cases) an example of the latter type of visual defect, is worldwide the most frequent cause of blindness [17]. The only real treatment for cataract is cataract surgery during which the impaired lens is replaced with an artificial implantable intraocular lens (IOL). In the European Union cataract surgery belongs between two most common surgical operations or procedures. In 2018 it was conducted 4,3 million times (within the EU). Only in Austria the number in the same year was 1360,2 cataract surgeries per 100.000 inhabitants. [12] Although cataract is prevalent mainly between elderly people, due to ageing of European population it is presumed the number of cataract surgeries will rise [13]. This is the reason why developing and enhancing already existing IOLs is indeed meaningful. If there is a tilt or decentration, these improved IOLs, however, may cause significant image aberrations and thus make the patient's vision even worse than if he had a simple IOL implanted. [39] [40] This paper continues in the work presented in [39] and aims for enhancing the optomechanical eye model (EM) for testing the IOLs by rebuilding the setup for measuring wavefront (WF) aberrations and including an imaging camera to enable for observing and checking the position of the IOL within the EM.

1.1 Human eye anatomy, histology, physiology and biophysics

The vision of human beings is provided by an eyeball and its accessory organs. The eye is situated in an orbit where it is wrapped in adipose tissue. Eyeball is a hollow sphere composed of two segments – anterior (cornea) and posterior (sclera). The diameter of eye is approximately 25 mm. For description of an eyeball terms as equator, meridians and poles are used (similarly to a globe). Poles are located in the most curved spots in anterior-posterior direction. Meridians connect poles. Equator is the longest circumference in a plane perpendicular to meridians. Straight line connecting both poles is called optical axis (OA). A line connecting fixation point and fovea centralis is called visual axis. Eyeball composes of a wall and its inner contents. The wall has three layers – outer, middle and inner layer. These three layers are described in subdivisions below together with the inner content of eye. Special focus aims on cornea, crystalline lens and retina as those are the most important parts for the model. Short note is

dedicated to accessory visual structures. Human eye anatomy is depicted in Figure 1. [7] [26]

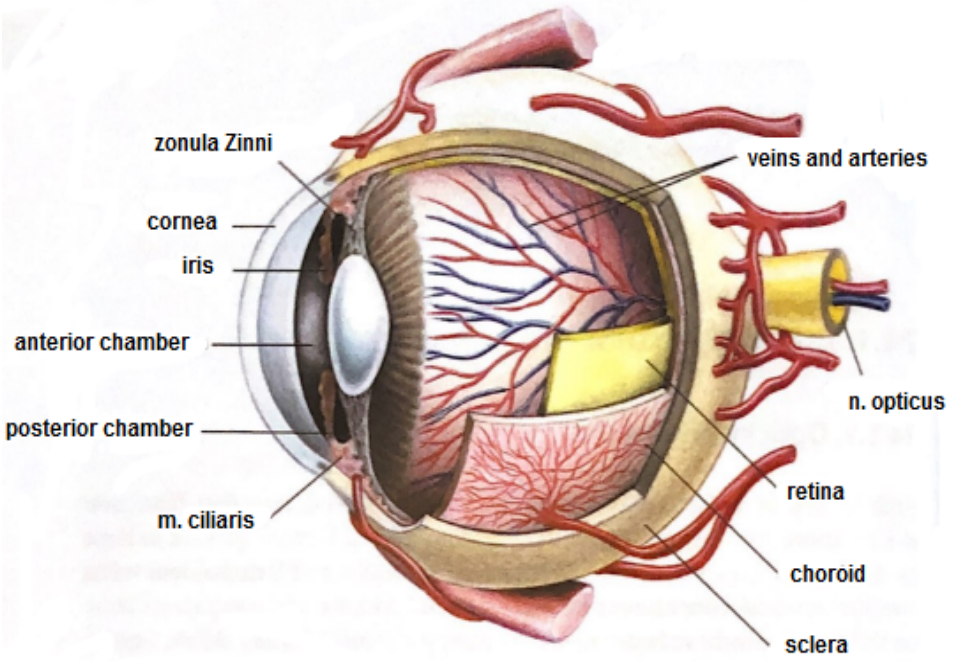

Figure 1: Human eye anatomy (adapted from [28])

Seeing actually means registering, processing and interpretation of electromagnetic radiation within 400-760 nm. The optical system (OS) of human eye is formed by these refractive components: cornea, aqueous humour, crystalline lens and vitreous body. The optical power of human eye accounts for +60 D. A real, inverted, reduced image of observed object is created on retina, more specifically on fovea centralis, by the OS of eye. Rays coming to eye from an object further than 5 m can be considered parallel and a point in this distance is called *far point*. The closest point to eye whose light rays still create a sharp image on retina is called *near point*. Width of accommodation is the distance between far point and near point. In conditions of good illumination, the eye can distinct two points whose rays are at angle of one angular minute. [7] [25] [26] [27] [28]

1.1.1 Wall of the eye

Outer layer of an eyeball

This layer is formed by a transparent cornea in the front, and a solid sclera. Sclera is 0,3-1,0 mm thick membrane which covers 4/5 of eyeball's surface and is formed mostly by collagen with additive elastic fibres. The surface of sclera is covered by a connective tissue which ensures the possibility of the eyeball's movement within orbit. This movement is provided by extraocular muscles. Small holes are present in the place where optic nerve leaves the eyeball as well as

in the place where cornea is attached to sclera. Supply by vessels is very moderate.

Cornea is a membrane that fills the remaining 1/5 of the eyeball's surface. It is embedded into sclera similarly as a glass into a watch. Cornea is transparent with width of 0,8-1,1 mm, slightly elliptical shape and with no vessels. Radius of curvature of cornea is 6,8-8,5 mm, vertical curvature being bigger than horizontal (compensated by brain center). Optical power of cornea equals 43 D, which accounts for 2/3 of total eye's optical power. Its body is composed of five layers – corneal epithelium, Bowman's layer, corneal stroma, Descemet's membrane and corneal endothelium. From the outside, the cornea is covered by a lacrimal film that includes lipids and glycoproteins and protects cornea from drying out. Epithelium regenerates well after injury (e.g. by UV radiation) but deeper injuries can cause cloudiness and scars. Corneal stroma forms 9/10 of the whole thickness of cornea being built of collagen lamellae, keratocytes and acid mucopolysacharides responsible for cornea's transparency. Descemet's membrane is highly refractive. Endothelium helps keeping the corneal body clear and transparent as it forms a barrier between cornea and anterior chamber filled with liquid. As no vessels are present in cornea, the nutrition is ensured by diffusion from anterior chamber. Cornea allows light of 310-2500 nm to pass into the eye and thus behaves like a UV filter. [7] [25] [26] [27] [28]

Middle layer of an eyeball

Middle layer of an eyeball is formed mainly by collagen connective tissue with high content of vessels. It also includes cells with pigment and smooth muscles. The layer is made up from three parts – iris, ciliary body and choroid. The last named, choroid, is a 0,1-0,2 mm thick membrane of brown and red colour located between sclera and retina. This component is formed by four layers and provides retinal cells with oxygen and nutrition. Ciliary body has in projection to sagital plane shape of a triangle with its base adjacent to iris and its sides to sclera and vitreous body. In frontal view its shape is an annulus. Three types of muscle filaments are present in ciliary body – regarding to the direction in which they are built. Two main muscles, Brücke's and Müller's muscle, are formed by these filaments and ensure accommodation of the crystalline lens through suspensory ligaments. Iris is a 0,2-0,4 mm thick membrane located in front of the crystalline lens (in the direction of light propagation). In the middle it features a hole called pupil. The pupil forms an aperture of the eye and its size is regulated spontaneously with regards to the amount of light falling onto eye. Its diameter affects eye's depth of field. Two muscles are responsible for this adjustment. Sphincter muscle is formed by smooth muscle cells around the pupil (having a circular shape). Dilator muscle is composed of myoepithelial cells present on the posterior side of iris (mostly radially arranged). Outer edge of iris is grown together with the ciliary body. [7] [26] [27]

Inner layer of an eyeball

Inner layer of eye wall is called retina. Retina has two distinct sections which differ in composition, thickness and function. Optical section of retina follows the surface of choroid and is

120-180 µm thick. Blind section of retina has 20-25 µm in width and it is grown together with ciliary body and iris. The optical section is a slightly transparent membrane which occurs to be of red colour due to choroid's shinning through. It originates in neural tissue thus having similar properties – neurons and glial cells together with pigment cells are present. Ten layers of retina can be distinguished in a microscope. Pigmental cells form outer layer of retina. These cells include black and brown granules of melanin and feature numerous microvilli whose function is to separate single rods and cones – photosensitive cells of retina. High illumination causes the granules to flow into the microvilli. Pigmental cells' connection to rods and cones is rather loose which can result in separation of retina (during eye injury, metabolic or vessel disease). Photoreceptor cells have thin and oblong shape and are called rods and cones. These cells convert light into electrical signal. The signal is generated due to oxidation-reduction changes to pigment molecules that the receptor cells include. The peripheral compartments (photosensitive) of these cells face the pigmental cells layer whereas their bodies with nuclei (central compartment) head towards the vitreous body and convert into axon. These cells convert light signal into electric potential and form the first neuron of the optical nerve. Human eye's retina features approximately 130 million of rods and 7 million of cones. Rods provide peripheral vision together with vision in dim environment (they mostly react to light intensity). They are spread across the whole retina (highest accumulation in the periphery) except for the fovea centralis. Their peripheral compartment resembles a rod due to its cylindrical shape, includes 600-1000 membranous discs and features photosensitive pigment – rhodopsin. Peak sensitivity of rods occurs at 500 nm.

Cone cells are indeed cone-shaped and serve for colour vision. They are shorter and more robust than rods. Instead of rhodopsin, cones contain iodopsin. Based on the variant of iodopsin included in them, three types of cones were described. Different types are more sensitive to different ranges of wavelengths (red: 550-570 nm, green: 520-540 nm and blue: 415-440 nm). The highest concentration of cones is in fovea centralis. In this spot retina has very small thickness as it only comprises of cones – this way light can travel to photosensitive cells with marginal losses which makes the fovea the spot of the sharpest vision.

Next layer of cells in retina comprises of bipolar cells that form second neuron of the optical nerve. According to the number of synapses we differ two types of bipolar cells. Diffuse type connects to several rods. Monosynaptic bipolar cells transmit signals from one cone to one ganglion cell. Third neuron of the optical path is formed by ganglion cells which can be as well as bipolar cells monosynaptic or diffuse. Axons of these cells go along retina's inner surface into the optic disc – place where the optic nerve leaves the eyeball through choroid and sclera. No photosensitive cells are present in this spot. Müller cells are the last type of cells present in retina. They are glial supportive cells that mainly participate on the structure of retina. Due to the reverse orientation of the photosensitive cells of retina with respect to light propagation within eye, human retina is described as inverse (as well as retina of other vertebrates). This feature enables for very precise and smoothly graded reaction to light stimuli. Also, convergence principal is present in the composition of retina – diffuse bipolar and ganglion

cells are responsible for this. One diffuse ganglion cell collects stimuli from around 140 rods (through several bipolar cells). [7] [25] [26] [27] [28]

1.1.2 Inner content of the eye

The inside of eye includes aqueous humour, crystalline lens and vitreous body. Aqueous humour is created in posterior eye chamber which it fills together with anterior chamber (altogether 0,2-0,3 ml). Normally this liquid does not contain any cells and is transparent.

Crystalline lens is a transparent, flexible body with diameter of approximately 10 mm and width 3,8 mm. The width can change up to 4,4 mm during accommodation for near objects. Posterior surface has bigger curvature than the anterior. Lens has optical power equal to +15 D. Similarly to skin, lens grows the whole life, although slowly. Contrary to skin, lens' oldest cells cannot be desquamated as they are located in the centre of the lens and new layers grow from the outside. [4] [9] It is located behind the iris in posterior eye chamber and incorporates no vessels. To the wall of the eye it is attached by zonular fibres (zonula Zinni). Starting from equator (largest circumference of the lens) these fibres connect the lens to the ciliary body and ensure the possibility of accommodation. When ciliary muscle contracts, tension in the fibres is relaxed and the lens arches by its own elasticity gaining more optical power thus accommodating for near objects. During this process the lens and the ciliary body move slightly anteriorly. The change in optical power is caused mainly by lens' front surface. Ciliary muscle relaxation makes the ciliary body to move posteriorly due to choroid's elasticity causing the zonular fibres to stretch which dilates the lens – accommodation for distant objects (rest state as the ciliary muscle is relaxed). The process of accommodation is illustrated in Figure 2. The lens' elasticity decreases with ageing resulting in seeing close objects worse (presbyopia). Besides the change in lens' shape, miosis and eye convergence occur during accommodation. Miosis (constriction of iris) increases the depth of field, eye convergence secures spatial perception.

Lens has three structural compounds – capsule, epithelium and fibres. Capsule represents an elastic, transparent, non-celullar envelope of the lens that is 10-20 µm wide and comprises of collagen and glycoproteins. Lens epithelium is only present on the anterior side of the lens. One layer of cells forms the epithelium, lateral cells are more longitudinal and convert into lens fibres. Lens fibres are of two types depending on where in the lens they occur. Fibres in cortex have nuclei and organelles whereas those in nucleus do not. In general, lens fibres are 7-10 mm long, 8-10 µm wide and circa 2 µm thick and originate from the epithelium. They are filled with special proteins – crystallins that determine their transparency. The distribution of these proteins also causes the gradient refractive index. The fibres are organised into concentric layered structure similarly to an onion.

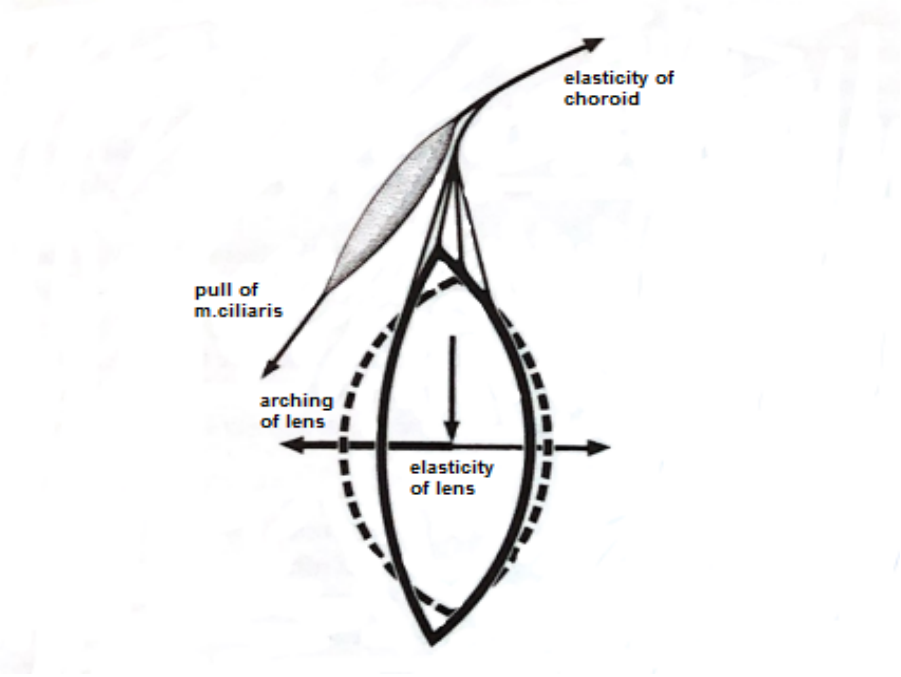

Figure 2: Accommodation of crystalline lens (adapted from [28])

Vitreous body is the last refractive ambient in the path of light inside an eye. It spans from the lens to the retina thus filling the vitreous chamber. This fully transparent gel-like substance is from 99 % composed of water, the rest stands for collagen and collagen fibrils. Very few cells are present in vitreous body. [7] [25] [26] [27] [28]

1.1.3 Ocular adnexa, lacrimal system and extraocular muscles

Two lids cover the eye – upper and lower eyelid. Eyelid composes of a layer of skin (outer face) and conjunctiva (inner face). These connect at the loose end of the eyelid where also eyelashes occur. Armature of eyelid is made of a collagenous disc. Conjunctiva is a mucous membrane that covers the inner part of eyelid and also the front side of eyeball up to cornea. It connects the lids with the eyeball. Lacrimal system of the eye includes lacrimal gland and lacrimal drainage system. The gland's secretion is spread on the eyeball and gathers in the medial corner of eyelid. Tears have antibacterial effect and moisten the eye's surface. From the eye's corner tears are drained through a drainage system into nasal cavity. Extraocular muscles are of similar structure as general striated muscle tissue. One neuron provides innervation for at most 3-5 muscle fibres thus securing very precise and graded reaction. In total six of these muscles per eye are responsible for eye movements. [7] [26] [27]

1.2 Brief overview of vision defects and eye pathology

The most common vision defects are refraction defects. [26] A few of these are described below briefly, more words are dedicated to cataract and its treatment description.
Astigmatism is an imperfection when the curvature of either cornea or lens differs in orthogonal planes (is unequal). Cornea is vertically curved more than horizontally (circa by 0,1 mm which changes the power by 0,5 D). This is considered to be normal condition. Pathological astigmatism means one of the orthogonal planes (horizontal/vertical) has optical power by 1 D different from the second plane. Myopia is a condition when light rays cross in front of retina creating blurred image. This is either due to high refractivity of cornea or lens, or more often due to longer eyeball. It is corrected with negative (concave) lens. Hyperopia causes light rays to cross behind retina also resulting in blurry image. Its causes are inverse to those of myopia. Hyperopia is corrected with positive (convex) lens. Presbyopia is caused by ageing of lens (as mentioned before). Lens looses its capability to curve resulting in difficulties with seeing near objects. Correction is done using convex lens. The ability of accommodation vanishes between 70. and 80. year of life. [25] [27] [28]

1.2.1 Cataract

The name of this disease comes from Greek and means "waterfall". Cataract is a state of crystalline lens characterized by its opacification or optical dysfunction. As stated in Chapter1, this condition is fairly common in population making it important also from economical point of view due to its overall treatment expenses. [9] Half of the population over 65. year of age has some level of opacity present in their lenses. Between 75 and 85 years this percentage rises up to 91 %. [29] Regarding the pathogenesis, histology, and prevailing opacity, cataract can be either cortical, nuclear, anterior subcapsular or posterior subcapsular. [9] [29] The most common cause of cataract is ageing although several other factors as drugs, toxins, trauma, heredity, radiation or systemic diseases can be the cause. [9]

Development of age-related cataract is connected with chemical changes to crystallins, decreased level of potassium, increased level of calcium and sodium and increased hydration of the lens. [29] So called sugar cataracts are caused by diabetes mellitus or galactosemia. In these cases patient's serum contains high level of either glucose (diabetes mellitus) or galactose (galactosemia) which results in formation of sugar alcohols in the lens cells. As these are not able to pass through cellular membranes, they accumulate thus causing the sugar (osmotic) cataract. [9] Approximately 75 % of patients with galactosemia acquire cataract during first few weeks after their birth. Any disease causing hypocalcemia can also be accompanied by cataract. [29] Cataract can occur when a systemic disease is present. Examples of systemic diseases that can induce cataracts are myotonic dystrophy, Wilson disease, Fabry disease or atopic dermatitis (as lens and skin have the same ontogenetic origin). [9] Complicated cataracts result from simultaneous ocular disease such as chronic uveitis, sarcoidosis, retinitis

pigmentosa, intraocular tumours or glaucoma. Around 10 % of vision loss in children is caused by congenital cataract. Traumatic cataracts might be of several causes. Laceration, rupture or contusion may cause cataract development within several days. [9] Penetrative eye injury sometimes leads to cataract, damage to capsular bag leads to cataract in most of the cases. Lens' dislocation within the eye is also often followed by cataract [29]. Siderotic cataract is name for cataract induced by iron foreign body present in eye for longer period of time. Considering the impact of radiation, only 250 cGy dose may be enough to cause cataract. [9] Exposure to UV radiation in the long term belongs to risk factors [29]. Electrical cataracts, albeit rare, are induced either by lightning strikes or electrical injuries. After lightning, usually posterior subcapsular cortex is affected whereas other electrical injuries affect anterior cortex. [9] Cataract may also originate in drugs or toxins. Long term treatment with high doses of corticosteroids is of the biggest importance. Intraocular steroids are also problematic. Amongst other drugs or toxins belong for instance naphthalene, mercury, anticholinesterase agents or cigarette smoke. [9] All of these types mentioned above can eventually lead to so called mature cataract (see Figure 3).

The diagnosis of cataract usually comes after patient's complaints on blurry vision or the physician notices a *"hazy view on the retina"* through an ophthalmoscope. Slit lamp examination serves to confirm the diagnosis. [21]

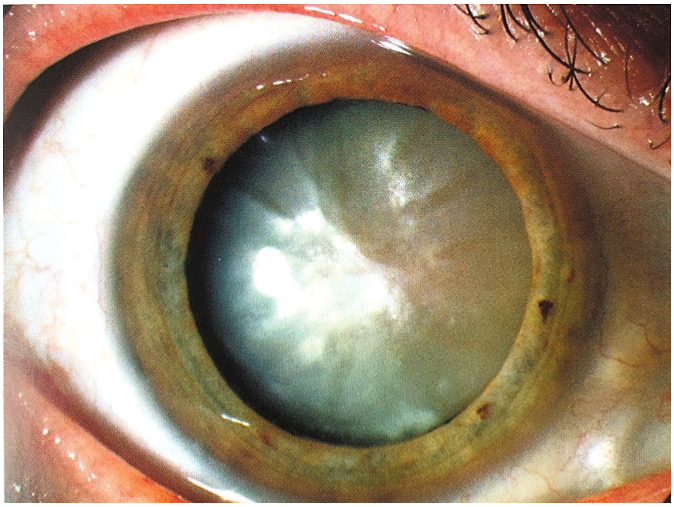

Figure 3: Cortical cataract – mature form [29]

Cataract surgery

Cataract surgery accounts for the most performed surgical procedure in ophthalmology. [20] Historically the oldest surgical approach (first references from 800 BC, India [29]) in cataract treatment was couching of the lens – releasing the lens from its position and moving it away from the visual axis. This was done with a sharp needle. The lens, however, remained in patient's eye. In some regions of Africa, this method is still in use. [20] [26] [29] Next method

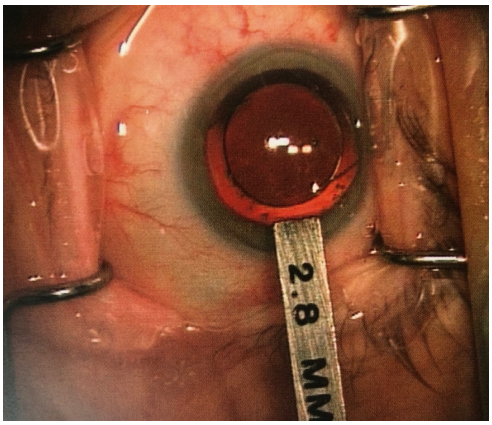

Figure 4: Acrylic IOL implantation through 2,8 mm incision. [29]

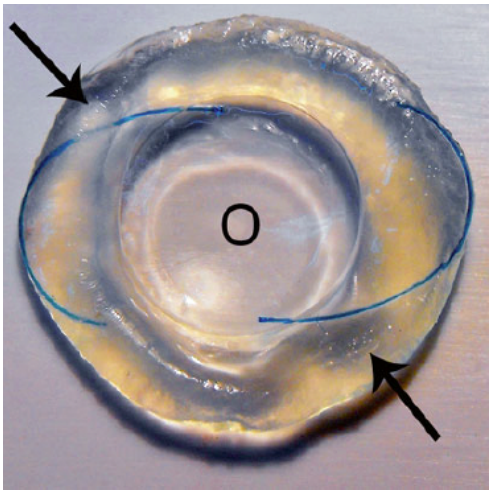

Figure 5: Illustration of IOL alignment in capsular bag. Central optic part (*O*) aligned with OA, haptics (*arrows*) hold the IOL within the bag. [4]

brought an improvement in removing the lens from patient's eye but without any replacement within the eye. The correction for insufficient optical power was done by strong glasses. [26] Intracapsular extraction uses cryoprobe to attach the lens with intact capsule to it by freezing. Later the lens is taken out from the eye through a big surgical hole. Correction is done also by spectacles. Nowadays, exctracapsular extraction is more common. During this procedure the capsule remains almost intact thus preventing retina from detachment. From the last mentioned method phacoemulsification evolved. [20] [29] The first surgery using this method was performed in 1967 by Charles Kelman. Two operating techniques exist – scleral tunnel incision and clear corneal incision, from which the latter is more convenient for the patient. Simplified steps of cataract surgery are: creating incision, injection of viscoelastic material, opening of anterior capsule, hydrodissection of the lens – lens' cortex and nucleus separation, nucleus splitting, emulsification and suction, cortex irrigation and aspiration, viscoelastic material injection, IOL implantation and irrigation of viscoelastic material. Suturing is not needed. Femtosecond laser was introduced to cataract surgery in 2009 providing alternative tool to execute some of these steps although due to increasing the cost and operational time, its use is a bit controversial. [21] [29] For the fragmentation, irrigation and aspiration a double-lumen cannula with an ultrasound tip is used. [4] As phacoemulsification is rather expensive method, in less developed parts of the world manual fracture of the lens' nucleus is used. [21] Already in the year 2007 cataract surgery was being performed *"without serious complications in 99 % of patients"*. [20] Figure 4 illustrates the surgical incision diameter, Figure 5 visualizes the IOL positioning within the capsular bag.

1.3 Implantable intraocular lenses

The first IOL of modern era was invented during the Second World War by a British ophthalmologist Harold Ridley. During several eye surgeries on a pilot with splinters from the cockpit in his eye, Ridley observed zero reaction of the pilot's immune system to these foreign bodies. Later he developed the first polymethyl methacrylate (PMMA) lens and successfully implanted it in 1949. This procedure became fairly common although approximately 15 % of patients suffered from postoperative complications such were severe hyphema, downward decentration, anterior and posterior dislocation or glaucoma. [4] [5] [19] PMMA as a material had many advantages as suitability for both one-piece and three-piece IOLs, perfect biocompatibility, hydrophobic surface and low price. Its downsides are mainly its rigidity and the need to sew the big incision necessary to implant the IOL. In 1950s hydrogel IOLs were developed as first foldable IOLs. Hydrogel has many properties in common with the PMMA, its major disadvantage is its price. First foldable IOLs also suffered from decentration. After the first silicone foldable IOL implantation in 1978, this type prevailed on the market. By substituting side-chain molecules of PMMA, a flexible acrylic IOL material is produced. [5] [19]

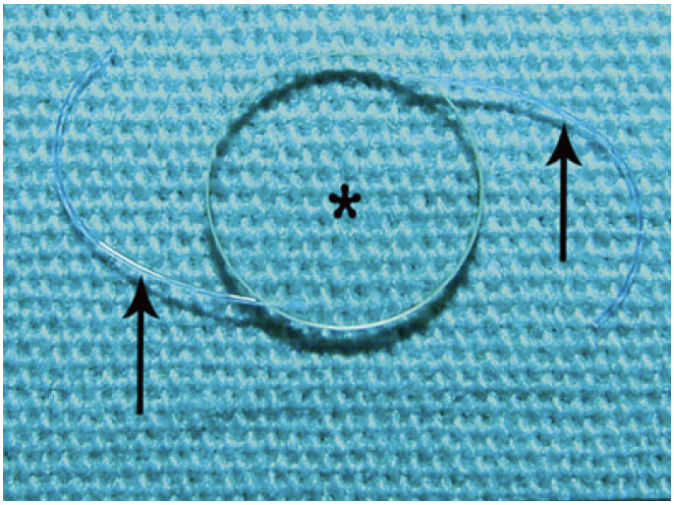

Figure 6: IOL design illustration: * marks the optical part, *arrows* point out the haptics [4]

IOLs are designed to avoid the need of spectacles after surgery [9] and using mathematical formulae which count with optical power of cornea or axial length of the eye. These and other parameters are measured during preoperative biometry (A-scan ultrasound, keratometry [21]). Resulting optical power after surgery should be emmetropic or mild myopic (-0,25 to -0,5 D) and the difference between operated and healthy eye's refractive power should not exceed 2-2,5 D. [20] [29] General requirements for IOLs are: biocompatibility, optical clearness, low weight, durability, ability to be sterilized or keeping inert state the whole life of the patient. [8] During cataract surgery, IOLs can be placed either into posterior eye chamber (preferred), or into anterior chamber. *Pseudophakia* is the name for an eye in which crystalline lens was replaced by an IOL. [20] [25]

IOL comprises from two parts – optical centre (responsible for refraction), and haptics (to hold the IOL in position inside the eye). [5] [20] [25] Following the material used for these parts, IOLs differentiate into one-piece and three-piece IOLs. An one-piece IOL is all made out of one material. Three-piece IOL has its central part fabricated out of different material than its haptics, which are connected to the central part later. With regards to the elastic properties of the IOLs, non-flexible and flexible types exist. Non-flexible, rigid IOLs require incision larger in size than the diameter of the IOL, which is why they are used rarely today. Flexible, foldable IOLs can be implanted through 2-3 mm incision while keeping the same final diameter as non-flexible IOLs. [4] [8] [20] [25]

Nowadays, two types of material are in use: acrylic and silicone. PMMA, being an example of the first group, is the only material utilised for manufacturing rigid IOLs these days. Foldable IOLs of acrylic can be hydrophobic or hydrophilic. Individual lenses' designs vary by the type of copolymer and have distinct physical properties. Hydrophobic and silicone lenses feature very low water content unlike hydrophilic lenses which include 18-38 % of water. Silicone lenses, having lower refractive index, must be thicker than flexible acrylic IOLs to achieve the same refraction. [5] [8]

Several types of design of IOLs exist. Aspheric lenses enable correction for spherical aberrations present in patient's eye. Positive spherical aberration is caused by cornea and negatively aspheric IOLs are used to resolve this in most of the patients. Neutral aspheric lenses have advantage in preventing visual worsening if tilted or decentered whereas corrective aspheric lenses may induce coma. Positively aspheric IOLs are used for patients after the laser-assisted in situ keratomileusis (LASIK) or photorefractive keratectomy (PRK) surgeries. [8] Monofocal lenses represent the most common type of IOLs and can either be designed to focus at near, intermediate, or distant objects. Their refraction is the least sensitive to displacement. Bifocal and multifocal IOLs provide focus for two or more distances. Diffractive, refractive or combination of apodized diffractive optics is used to machine these lenses. Perfect eye health is needed to enable the patient for this type of lens but even in such cases patients may suffer from reduced contrast sensitivity or halos. Accommodative IOLs are supposed to provide accommodation. This can be achieved either by forward movement of the lens or by change in diameter of deformable IOL. One millimeter of forward movement however changes the optical power only by 1,3 D. Toric IOLs are used to correct for astigmatism. Their orientation within the eye is essential as displacement can decrease the vision quality. Alignment during surgery can be done by junctions at the border between optic and haptic part. Resulting alignment quality is influenced by preoperative marking accuracy, intraoperative aligning, lens removal success and the time the IOL and its haptics have to unfold properly. [8] [20]

Design and materials for manufacturing of the IOLs is under constant development.

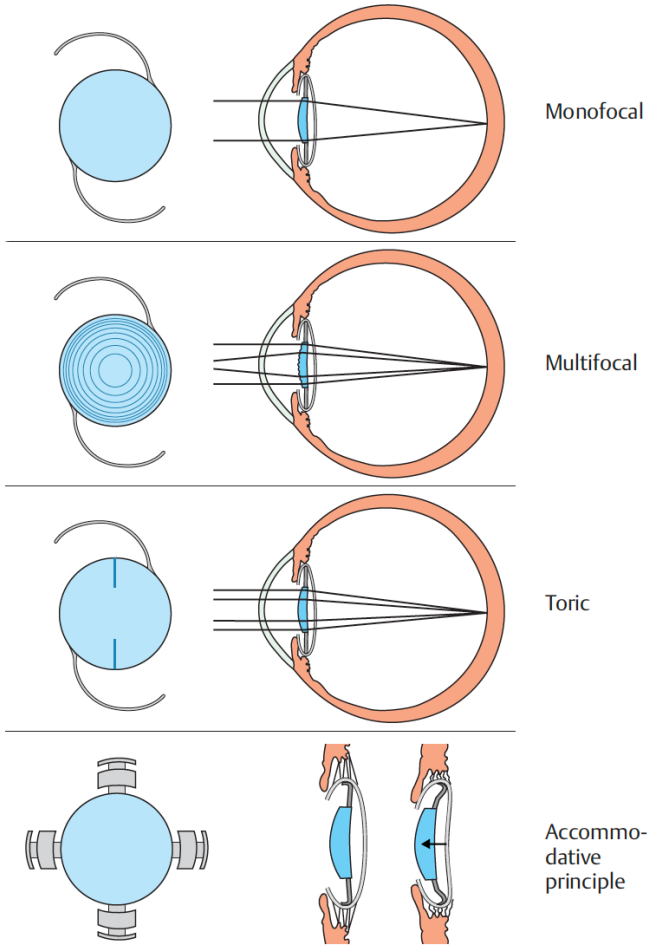

Figure 7: Different designs of IOLs [20]

1.4 Theoretical foundations of optics

In this chapter, the fundamental principles of optics are discussed with a focus on concepts which are related or used within the EM setup. Special attention is dedicated to image aberrations.

1.4.1 Light propagation

The propagation of light through a medium is described by using rays and waves. A light ray, being represented by a line normal to the WF, is the path that light follows. If the medium in which the light propagates has constant refractive index, then the rays are straight lines. The term *light ray* can also be understood as the x-axis of the electromagnetic wave of light. Ray tracing is a powerful tool for OSs description. This process is an iterative procedure during

which the coordinates of intersections with individual surfaces of the OS and direction changes at these boundaries are calculated. However, the use of ray optics is limited by the wave character of light mainly represented by diffraction and interference. [15] [31] [32]

Geometrical WF, which can be calculated using light rays, represents the surface with equivalent optical path length (OPL). In homogeneous media OPL is calculated as follows:

$$OPL = \sum_i n_i \cdot s_i \tag{1}$$

where n_i are refractive indices of individual media and s_i the lengths of the rays in these media. Refractive index is described as:

$$n = \frac{c_0}{c} \tag{2}$$

where n is the refractive index of given environment, c_0 is the speed of light in vacuum, and c is the speed of light in given medium. This way the term WF is associated with the transient time of rays through the media and can be defined as a surface with the same transient time of light. During the propagation of light through space the WF is deformed and phase variations emerge. This is the cause of image aberrations. [15] [23] [31] [32]

1.4.2 Basic optical phenomena

Refraction

In optics, refraction is a fundamental phenomenon which occurs at every boundary of optically distinct environments. Refraction describes deflections of the light propagation direction and is characterised primarily using the refractive index, as it was defined in Equation 2. To numerically determine the change of direction, Snell's law applies:

$$n_1 \cdot \sin\alpha = n_2 \cdot \sin\beta \tag{3}$$

where n_1, n_2 are the indices of refraction of first and second medium, respectively, α, β are the angle of incidence and the angle of refraction, respectively. [15] [32]

Reflection

Reflection, as well as refraction, happens on the boundary of two optically different environments. The quantity used to describe reflection is reflectance. Reflectance depends on the refractive indices of both media, angles of incidence and refraction, or polarisation. If the light travels from an optically thicker environment into a thinner one, total internal reflection may occur if the angle of incidence equals or becomes larger than the critical angle. Reflection of light hitting high-index medium after travelling in low-index medium causes phase change of 180°. Inverse order of indices causes no change to the phase of the wavelength. Reflection followed be interference can be the cause of ghost images creation or high light intensity spots

presence. It also has impact on the overall intensity, as this is reduced during the reflection of the light. [15] [32]

Dispersion

The refractive index of a medium is not constant but dependent on the wavelength. This effect is called dispersion and is the cause of chromatic aberration formation. Considering normal dispersion, the refractive index diminishes with the increase of the wavelength resulting in higher refraction of ultraviolet part of spectrum, and low refraction for infrared part. To characterise an optical material, so called V-number is regularly used:

$$V_e = \frac{n_e - 1}{n'_F - n'_C} \tag{4}$$

where n_e, n'_F, n'_C are the refractive indices of the material at wavelengths corresponding to the Fraunhofer lines *e, F'* and *C'*. [15] [32]

Transmission, absorption

The intensity of light transmitted in an OS not only falls down with the reflections on surfaces but it is also diminished exponentially by absorption within the optical media. Lambert-Beer law is utilised to express this phenomenon numerically:

$$I = I_0 \cdot e^{-x \cdot \alpha} \tag{5}$$

where I is the resulting intensity in position x, I_0 is the initial intensity, and α is the absorption coefficient, which characterises every optical environment. Internal transmission of light is given by the ratio of light intensity in observed location and the initial intensity. Absorbance is then given by:

$$A = 1 - T \tag{6}$$

where T is the internal transmission. To specify the propagation of light through an optical component, both reflection and absorption have to be considered. [15]

Interference

Interference affects the light as light can be defined as an electromagnetic wave. Superposition of waves is the cause of interference. Constructive and destructive interference are the two special cases of interference which lead to amplification or moderation of the wave's amplitude, respectively. Total destruction of the wave can be achieved in destructive interference. Both of these special cases are used in optical components, e.g. in coating layers. [15] [32]

Diffraction

Another mechanism originating from the wave nature of light is diffraction. In general, by diffraction we call the ability of light of reaching areas that are hidden behind an obstacle. Using the ray optics to describe this phenomenon is not possible as the wave theory has to be applied. Depending on the shape of the aperture (obstacle), specific diffraction pattern emerges as a result of superposition of the waves that are propagating behind the obstacle. Airy disc is the name for rotationally symmetric diffraction pattern of a circular aperture. Ray optics suggests that by imaging an object point one can achieve infinitely small image point in the image plane. In reality, Airy disc appears instead. As the diameter of the Airy disc is dependent on the diameter of the aperture stop, this becomes a crucial feature of the system having impact on its resolution. The Rayleigh criterion states that *"two image points can be clearly distinguished if the distance between the corresponding discs is equal to or higher than half the Airy disc diameter"* [15] [32]

1.4.3 Imaging with an optical system

To describe imaging with an OS, several approaches can be applied. These are paraxial (Gaussian) model, geometric-optical imaging and wave imaging. Paraxial imaging (also ray optics) is significantly simplified, ignores the wave nature of the light and counts with restricted field of view (FOV). Geometric-optical imaging applies to larger fields of view and aperture heights and is sufficient for large amount of optical setups. Although perfect if modeled with the two above mentioned approaches, OS still suffers from limitations of resolution. These and other wave phenomena can be described only by wave optics. Also laser propagation in an OS is described by wave optics as the paraxial model is not suitable. [15] [23]

One of the key properties of an OS is its symmetry, which can be of several degrees. Rotational symmetry of an OS is determined by OA which corresponds to the z-axis of the coordinate system. Object and image lie in planes orthogonal to the OA in object and image space respectively. The plane to be imaged by the OS is called the FOV and is defined by a field stop located at the image plane. To regulate the amount of light passing through the OS and to define the light beams well, an aperture stop is used being the vital element of the OS. In general, the aperture is considered to be circular, perpendicular and centered with the OA. An entrance pupil is the image of the aperture in object space, similarly, an exit pupil is the image of the stop in image space. Both of these images might be real or virtual. The location of the aperture stop affects the presence and type of image aberrations. Stop shifting, moving the aperture stop along the OA while keeping the f-number (fraction of focal length and the entrance pupil diameter) constant, has direct effect on creation of the aberrations. [15] [23]

To describe an imaging optical component or system, several types of planes, points and rays are used. Principle planes, two virtual planes orthogonal to the OA, are used to describe refraction of an optical element. In these planes refraction theoretically occurs, although practically it happens on the surfaces of the material. One of the two planes is located in object space

(*H*), the second in image space *H'*. Principle planes can also be located beyond the physical borders of an optical element. Principle points are the intersections of the principle planes and the OA. Focal points are the points of intersection of rays coming from infinite distance and parallel to the OA. These points lie on the OA. Nodal points are utilised as the principal points for tilted incidence of light. [15] [31] [32] Meridional plane is a plane containing the OA. A marginal ray is a ray going through object point located on OA and through the edge of the aperture stop. A chief ray is a ray passing through the aperture stop's centre and the edge of the FOV. The chief ray always lies within the meridional plane. [23] [31] [32] Using vectors, a ray can be described by a field vector $\vec{H}$ (located in the object plane) and an aperture vector $\vec{\rho}$ (located in the exit pupil plane). A point of origin of particular ray is specified by the field vector, whereas the aperture vector determines the point of intersection of the ray with the exit pupil plane. The angle between these two vectors is φ. [31] [32]

There are several sign conventions to be followed so as the equations describing an OS give as accurate results as possible. These are as follows:

- Height of a ray is positive if measured above the OA and negative if under the the OA.
- Distance to the right-hand side from the plane of reference is positive, whereas distance to the left is negative.
- If a counter-clockwise movement from the OA is to measure the ray's slope, then the slope is positive. Otherwise it is negative.
- In object space, unprimed quantities are used, in image space primed quantities describe the system.
- Chief rays are described by barred quantities, marginal rays by unbarred quantities.

[23] [31] [32]

1.4.4 Aberrations

Aberration is *"a departure from ideal behavior"*. [31] In reality, having an entirely aberration-free optical component or system is unfeasible. Furthermore, often not only one but several aberrations occur in the system. Due to that, an image might not even lie on a true plane but rather on curved surfaces like a paraboloid. [15] [32] The theory of aberrations is mainly related to the concepts of rays, optical path and geometrical WF, as these were described in previous chapters. [31] In this section, the most common image aberrations are discussed.

Spherical aberration

Being a basic image imperfection, spherical aberration is caused by the use of spherical surfaces within an OS. Focal length is dependent on the height of a ray (from the OS) as for different heights different angles of incidence and thus also different angles of refraction apply.

The closer to the OA the ray travels, the closer its focal point lies to the paraxial focal point. Longitudinal and lateral spherical aberration can be measured. With constant f-number, spherical aberration is influenced by the object position and lens' shape. [15] [32]

Coma

As the images affected by this aberration resemble a tail of a comet, this defect was named *coma*. It results from the property of real OSs in which the rays usually are not exactly parallel to the OA but inclined. This aberration especially appears while imaging high objects at short distances, as this means leaving the paraxial space. With regards to the central axis of the light rays bundle, the angles of incidence are unsymmetrically distributed, which results in a comet-like asymmetry in the image plane. Coma can be corrected by changing the position of the aperture stop to the so-called natural stop position. Besides the position of the stop, coma also depends on its diameter and distance from the image plane. [15] [32]

Astigmatism

This aberration is described as that the optical component features two different focal points for two different orthogonal planes – meridional and sagittal. The cross-sections of the lens in these planes are of dissimilar shapes and radii of curvature. Due to this, two line images are formed. The best result is found in between of these and is called the circle of least confusion. This, however, also features blurred image. The further from the OA the object point is, the higher the astigmatism. Power and shape of the lens influence the astigmatism the most together with its distance from the aperture. Anastigmatic or apochromatic lenses can reduce the effect of astigmatism. [15] [32]

Distortion

Distortion appears while imaging object points located off the OA and, similarly to coma, depends on the aperture stop placement. It is the result of variations in magnification within the image plane. The magnification can either decrease or increase with growing image height, the geometry of the object is thus not transmitted well by the OS and is distorted. Either way, with growing object height distortion increases. Two types of distortion exist: positive (pincushion) and negative (barrel) distortion. [15] [32]

Chromatic aberration

This aberration type is caused by dispersion of light. As a consequence, OSs feature dependence of focal length on particular wavelength. This mechanism is called as longitudinal chromatic aberration. Lateral chromatic aberration is the name for a secondary effect of the

image height being wavelength-dependent in particular image plane as this plane can be determined for each wavelength separately, if not corrected. A halo surrounds a bright image dot of an axial object point in presence of chromatic aberration. [15] [32]

Wavefront aberration

This section outlines another approach to describe the effect that an OS has on the quality of an image. Aberrations of a WF are determined as departures of the observed WF from a reference, e.g. planar or spherical, WF. Ideal image point is created by a spherical WF with centre in this point. To quantify the deviations from an ideal reference WF, RMS (root mean square) or PV (peak-to-valley value) can be used. Characterisation of an OS can be obtained by measuring the WF deformation in the exit pupil plane and for corrected systems is taken as *"the most useful measure of the image quality"*. Considering a rotationally symmetric OS, its WF aberration function is dependent on the height of the object, or image (from the OA), and pupil coordinates (r, θ) of a point within the exit pupil plane. [15] [23] [32]

Other image defects

Vignetting is characterised by diminishing brightness of the image in direction from its centre to the peripheries. Causes are mainly of mechanical or optical character. Ghost images emerge from parasitic light within the OS that originates from reflections and scattering. [15]

Zernike polynomials

To evaluate the performance of an OS, being able to describe the aberrations present within this system is a valuable tool of doing so. Amongst the available methods belong various mathematical polynomial, such as aberration, Zernike and WF polynomials. As within the proposed EM setup in this thesis the Zernike polynomials are used, only these will be further discussed.

Based on the theory of Fourier series, Zernike polynomials are defined as a *"set of infinite series of orthogonal polynomials"*. Counting with two variables, azimuthal angle φ and normalised radial distance ρ, these polynomials can be used to describe a two-dimensional WF. Even and odd Zernike polynomials exist, the even being defined as:

$$Z_n^m(\rho, \varphi) = R_n^m(\rho) \cdot cos(m\varphi) \tag{7}$$

and the odd:

$$Z_n^{-m}(\rho, \varphi) = R_n^m(\rho) \cdot sin(m\varphi) \tag{8}$$

where $m, n; n \geq m$, are positive integers, $R_n^m \rho$ is the radial polynomial. The WF may then be expressed as:

$$W(\rho,\varphi)=\sum_{m=0}^{\infty}\sum_{n=m}^{\infty}[A_n^m Z_n^m(\rho,\varphi)+B_n^m Z_n^{-m}(\rho,\varphi)] \tag{9}$$

Using the orthogonality of the Zernike polynomials, A_n^m, B_n^m coefficients can be determined. Describing a WF is usually done by using first several of the Zernike polynomials terms with respect to the desired accuracy. The number of terms used for a WF fitting should be appropriate to the complexity of tested OS or surface. Each one of the Zernike polynomials has some optical interpretation, however, the higher the order is, the more difficult it becomes to explain this meaning. A few first Zernike polynomials are listed in Table 1. [6] [33] [39]

Table 1: Several first Zernike polynomials with their interpretation

Number	Radial Degree *n*	Azimuthal degree *m*	$Z_n^m(\rho,\varphi)$	Optical interpretation
1	0	0	1	piston
2	1	1	$2\rho cos(\varphi)$	x-tilt
3	1	-1	$2\rho sin(\varphi)$	y-tilt
4	2	0	$3^{0,5}(2\rho^2-1)$	defocus
5	2	2	$6^{0,5}\rho^2 cos(2\varphi)$	oblique astigmatism
6	2	-2	$6^{0,5}\rho^2 sin(2\varphi)$	vertical astigmatism
7	3	1	$8^{0,5}(3\rho^3-2\rho)cos(\varphi)$	horizontal coma
8	3	-1	$8^{0,5}(3\rho^3-2\rho)sin(\varphi)$	vertical coma

1.5 Eye models

The necessity for models of human eye was before mainly related to the need of understanding the refraction, the imaging process or the effect of glasses and contact lenses on the human eye. Nowadays, EMs gained importance within various eye surgery processes or eye prosthetic implants development and testing. First models of human eye were designed within the paraxial region and work mainly with spherical surfaces, whereas today wide-angle models which may include aspheric surfaces, accommodation or gradient refractive indices are being developed. Three common paraxial models are depicted in Figure 8. [2]

One of the first EMs was the Helmholtz-Laurance model. Developed by Helmholtz and modified by Laurance, this model features all refractive surfaces that a real human eye has. [1] Donders' reduced eye is a simpler model which utilises only one spherical surface (with diameter of 6,0 mm) to simulate the whole refractive system. Two homogeneous environments are incorporated. Donders' EM cannot be used for calculations where high precision is needed as it is too simple. [25] Later, Gullstrand proposed a new model featuring a cornea with two

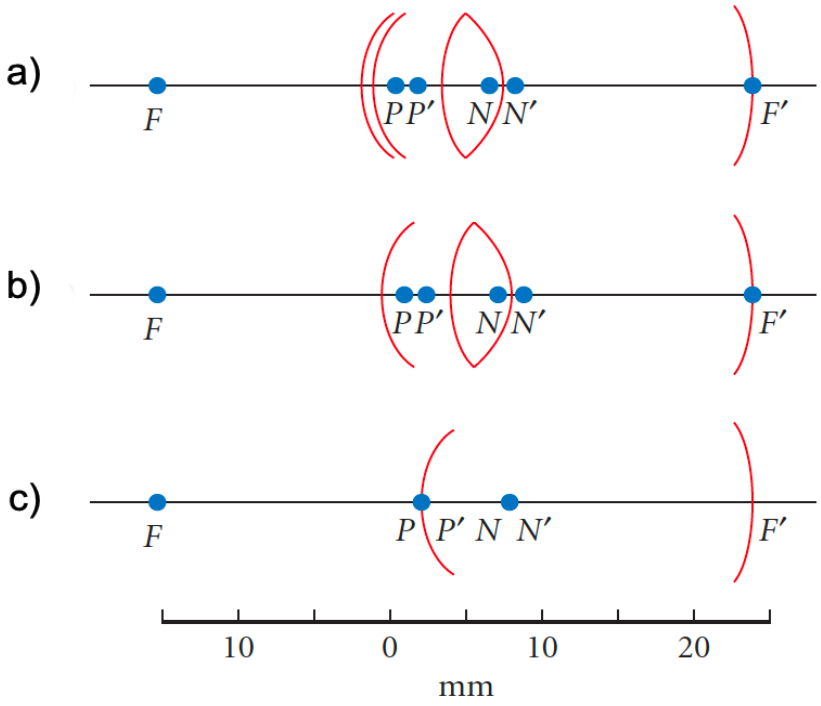

Figure 8: Comparison of three paraxial EMs. F, F'; P, P'; N, N' are focal points, principal points and nodal points, respectively. *a)* Le Grand schematic eye, *b)* Emsley simplified schematic eye, *c)* Emsley reduced eye (adapted from [2])

surfaces. Difference in cornea's front and rear surface or difference in refractive index in the parts of the crystalline lens are not taken into account, however, front and rear surfaces of the lens are include thus enabling the use of this model for the calculation of the power of IOLs. [1] [25] Emsley EM features only one refractive surface being one of the simplest models used nowadays. More recently, Greivenkamp invented a model with four aspheric surfaces based on in vivo corneal parameters measurements. To these days perhaps the most anatomically and optically accurate EM is represented by the Liou and Brennan EM proposed in 1997. Their model incorporates the tilt of visual axis from the OA as well as decentration of the pupil, gradient refractive index of the lens and dispersion. [1] This EM is used within the standards for IOLs – ISO 11979-2 [18] and thus also within the thesis [39], where the EM to be used in this paper is developed being based on the Liou and Brennan numerical model.

1.5.1 Initial eye model setup description

The setup that is being modified within this thesis was formerly created as a reaction to insufficient and incomplete testing standards for IOLs. [39] These standards are specified in ISO 11979-2. In the time of writing this thesis, ISO 11979-2:2014 was in effect (as well as in the time when the former model eye was created [39]). The EM presented in [39] was designed to mimic human eye's anatomy and physiology *"as close as possible"* [39]. PMMA cornea

(custom-made) features average spherical aberrations of the natural cornea, although having different refractive index and thus a slightly different shape. Decentred pupil and angular deviation between optical and visual axes are incorporated within this model. Tilt and decentration (shift) of an IOL, as well as the combination of these parameters, can be tested. [39]

The EM is encased into a plastic box with precision threads for the cornea and retina models in front and rear part, respectively, with grooves for alignment of the pupil slide-in plates and another grooves for the tilt-shift device. The box features holes for registering pins on the inner side, and registering pins on the outer side of the bottom. The inner holes serve for the tilt-shift device alignment, the outer pins for aligning the model on a stage and securing the 5° tilt of visual axis. Before each measurement, the tested IOL is placed into a holder within the tilt-shift device. This holder is 3D-printed for each IOL. The centre position of the IOL is then checked utilising a stereo microscope. Another inspection is done by a "machine vision" setup (imaging camera with a telecentric lens) to assess the position of the tilt-shift unit within the EM. The process of tilting and shifting during the measurement is automated and secured by two small actuators on the tilt-shift unit. The retina model optically connects the EM with measuring devices and is made of 1 mm thick BK7 glass. [39]

With regards to their purpose, three setups were developed in [39] using the same EM. These are: a setup for measuring the modulation transfer function (MTF), WF aberrations measuring setup, and a demonstrative setup. Within the presented thesis, the second setup is being modified therefore is described more in detail here and is depicted in Figure 9. A laser is used as the illumination source (not included in Figure 9) with its beam being expanded by a beam expander (BE) to illuminate the whole pupil of the EM. The EM is positioned with the 5° physiological tilt. The light is focused onto the retina by the cornea and the tested IOL, and then a relay lens is utilised to transform the spherical wave to a parallel wave behind the EM and to image the pupil plane onto the microlens array of the Hartmann-Shack wavefront sensor (WFS). During the measurement, the tilt-shift device is controlled by a MATLAB custom program. The same program also ensures the acquisition of the first 15 Zernike polynomials from the WFS software and calculates the MTF. The weakest link within this setup is the relay lens due to its manufacturing tolerances. [39]

1.6 Problem statement

Several factors do not favor the usage of the WF measuring setup as described above. The setup is not completely physiological as the WF is detected behind the EM which in reality would not be feasible. This also implies, and was noted in [39], that if a scattering retina model was used in a double-pass setup, this would enable for examining the EM with devices from clinical ophthalmology. Another property of the presented EM system to be improved is the "machine vision" inspecting element which could be implemented within the measuring setup and thus the amount of manipulation needed in the whole process accompanied with possible space for errors could be reduced. Next downside to be covered is the necessity of changing the pupil

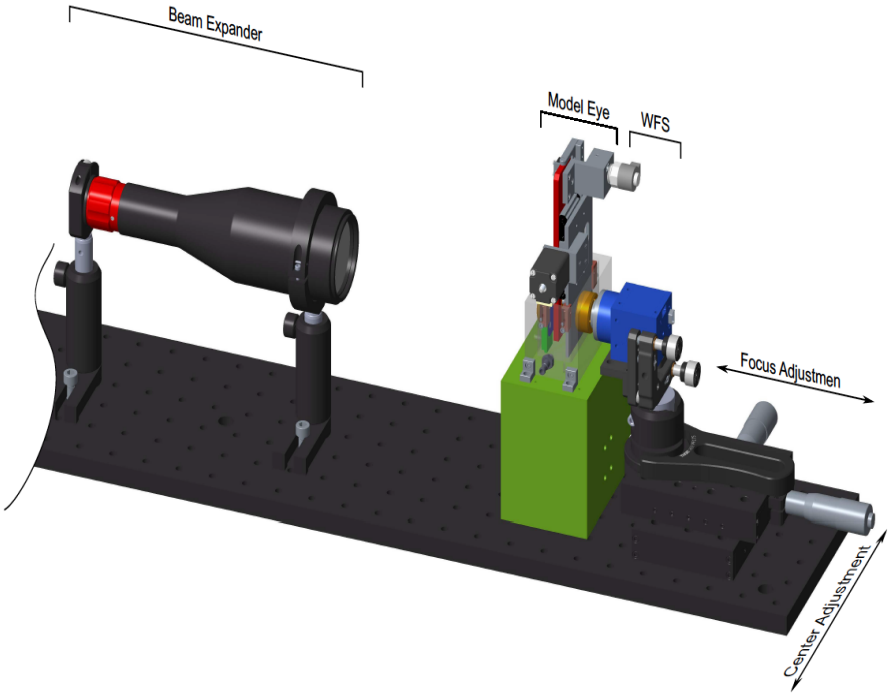

Figure 9: The WF aberrations measurement setup from [39]

slide-in modules to simulate the conditions of the photopic and scotopic vision. Resolving this issue should allow for keeping the focal length (axial length) of the EM constant during the whole measurement procedure, again, reducing the errors emerging from frequent manipulation with the model. The last two disadvantages that offer space for improvement are the geometrical aberrations caused by the relay lens located behind the tilted EM (retina also tilted), and the amount of noise in the WFS's signal blocking the use of the higher order Zernike polynomials. [39]

2 Methods

In this chapter, the development of a new enhanced EM setup that could resolve the issues listed in Section 1.6 is described in detail. The steps underwent during the whole development process, including modelling the setup in a CAD software, numerical simulations in optical design software, calculating the EM parameters, manufacturing the retina model or, in the end, assembling the proposed EM setup, are discussed below.

2.1 Enhanced setup description

A single-pass setup presented in [16] was adapted for the purpose of this thesis. The setup described in [16] was developed with the objective of diagnosing the stadium of cataract on living patients, however, the concept used to achieve this goal was found to be beneficial and eligible to cover most of the disadvantages of the former EM setup (Section 1.6). Figure 10 illustrates the working principle of the setup, Figure 11 shows the outline of this setup. This approach, applied for the EM setup improvement, has some properties of both the double-pass and the single-pass setups that were introduced in [39] but in the end not used. The similarity with the first one (the double-pass) is in the laser and WFS mutual perpendicular position. Furthermore, both (together with the whole setup) are located in front of the EM. The difference here is in the fact, that the proposed EM character is a single-pass, as can be deduced from [16]. This is because the light focused on the retina model should become a point source due to sufficient amount of back scattering whereas in a double-pass configuration, the light is reflected from the retinal surface (this is not desired). Also, the placement of the laser source and the WFS is reversed compared to the double-pass setup from [39]. The resemblance to the unused single-pass setup from [39] is in utilising a point source located in the image focal point of the EM. The adaptation of the setup in [16] included making of several major changes. These can be seen by comparing Figure 11 and Figure 12. The working principle of the new enhanced EM setup for testing of the IOLs will be presented now.

The collimated laser beam of 3,5 mm coming out from a laser diode is the source of the light for both the WF aberrations measurement and for the imaging of the IOL within the tilt-shift device in the EM. This laser beam is immediately after leaving the source expanded by a BE to a new, wider diameter of approximately 37,5 mm. This beam is then narrowed by an iris diaphragm to fit the front entrance hole of the EM. On the way to the inside of the EM, the light passes through the first beam splitter with no intended effect on the measurement. A side effect is the loss of half of the intensity by the 50:50 splitting ratio of the beam splitter. Then,

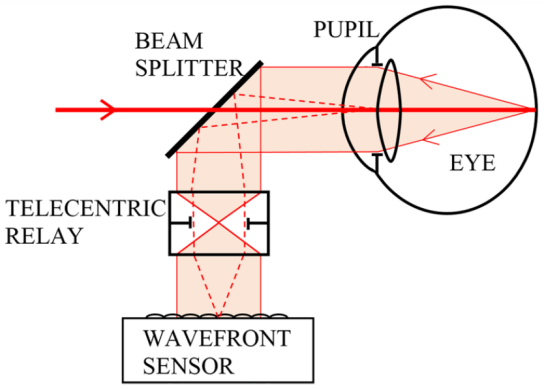

Figure 10: The principle of the cataract stadium assessing method presented in [16] and adapted for the purpose of this thesis

the light entering the EM is refracted by the cornea model and after that enters the human eye-simulated environment – water – within the EM. The light is refracted again by the tested IOL and finally lands on the retina model. Due to the axial length calibration (done by adjusting the retina model distance beforehand), a bright spot is created in the focal point of the EM. This spot becomes, as a result of scattering, the point source for the back illumination of the IOL. The scattered light travels through the water within the EM, the IOL and cornea, and leaves the EM while carrying information about aberrations created within this OS. The first beam splitter directs this light in the direction of the sensor cameras. Again, half of the light is lost as it travels back in the direction of the laser source. The second beam splitter divides the light beam into two bundles, one of them going through a 0,75x telecentric lens and then falling onto a microlens array of the WFS, second bundle passing 0,5x telecentric relay and finally hitting the sensor of the monochromatic imaging camera.

If compared to the setup in [16], this new proposed model does not use:

- The collimator lenses – laser source provides collimated light beam.
- The second light source of a different wavelength – one laser diode ensures illumination for both applications.
- The fixation target – not needed as the model is for *ex vivo* testing of the IOLs.
- The long pass mirror – this is related to the previous point.
- The band pass filter – as it is not necessary.

2.2 Development of a CAD model

To be able to better visualize the whole EM setup to be constructed, a CAD (computer-aided design) software was used to develop a so called CAD model first. This approach has sev-

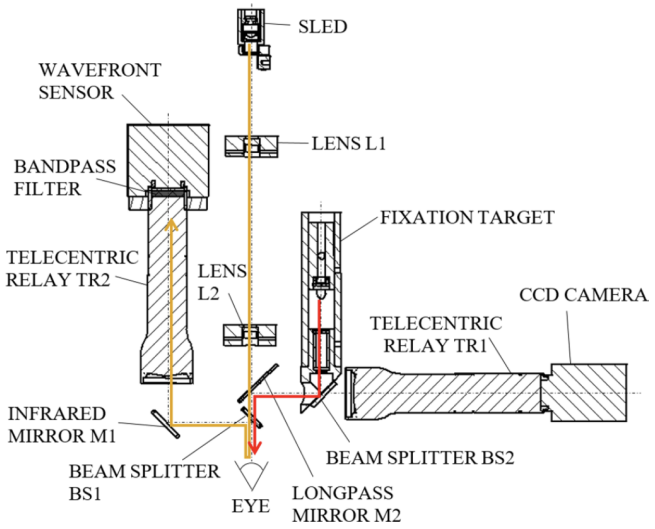

Figure 11: The cataract-assessing setup illustration with description of its parts [16]

eral other benefits excluding the visualisation. Amongst these advantages, the most crucial (following the author's opinion) is the ability of moving the components within the time range of seconds. This approach thus saves a plenty of time only by enabling the user to modify alignments that would take minutes, or hours in some cases, to do so with real components. Furthermore, the components are available for download on the websites of the manufacturers. Another advantage of modelling in CAD software is the possibility of creating functional joints between various components. This way the realistic movement that the components may perform in reality can be simulated. The last but not the least important benefit is the measurement feature of this software which was used often. The setup in [16] (Figure 11) was taken as a rough outline. During the design process, several versions of the CAD model were developed. These versions were using multiple different components, mostly those of mounting purpose, and simulating number of distinct mutual positions of these. Several crucial construction notes were deduced based on a simple observation of the CAD model or on the measurements performed on it during or after the development. These were e.g. the position of the imaging camera relative to the BE and to the iris diaphragm, the positions of the mounting stages for the two beam splitters in front of the EM, the orientation in space of the same stages, or the distance of the 0,75x telecentric relay from the EM. The last parameter was measured multiple times as it was essential to know which working distance (WD) would be feasible. Finding all of these positions and distances resulted in the definitive version of the CAD model which is depicted in Figure 12 (including description), Figure 13 (top view) and Figure 14 (all four side views).

The whole CAD model was developed in Autodesk Fusion 360 (CAD/CAM/CAE software). Excluding the EM box and its base plate, all the other models of the real components were downloaded from the web pages of their manufacturers, as it was mentioned above. Consid-

ering the EM, this CAD model component does not reflect the reality perfectly well as it is not needed for the purpose of the CAD model. Thus only the size of the EM box and the hole for the cornea and retina are featured.

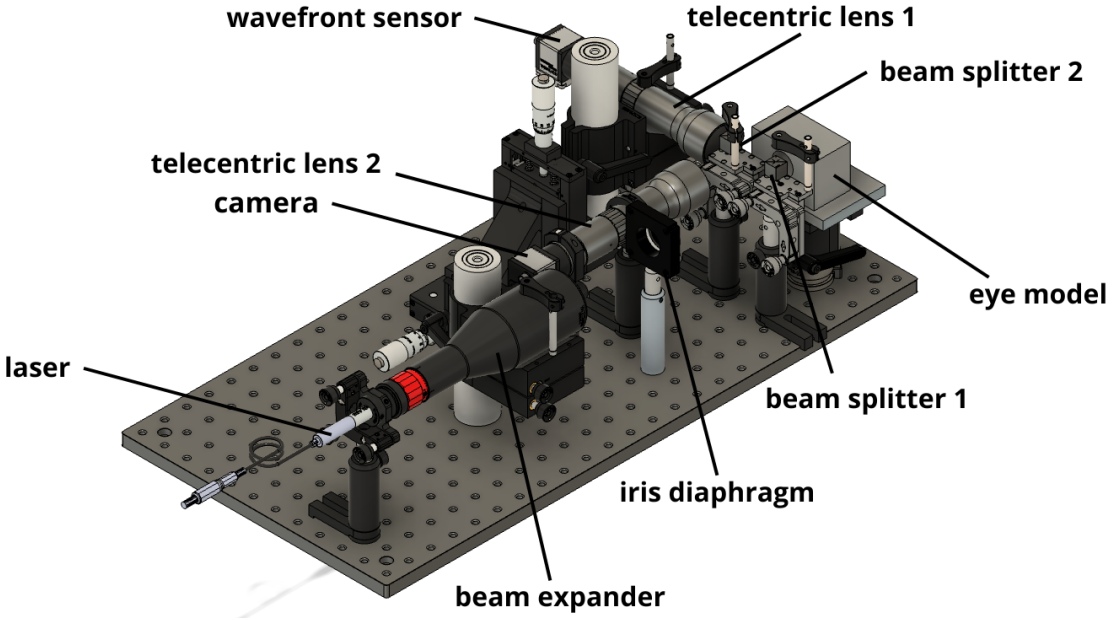

Figure 12: CAD model of the EM setup with labeled parts

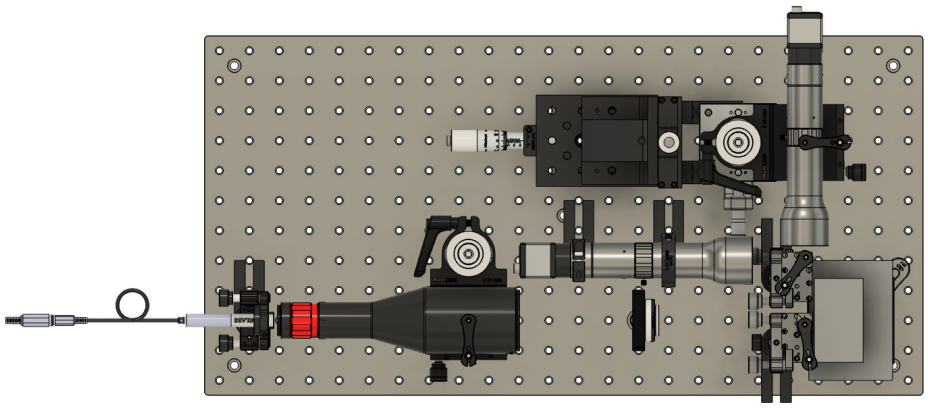

Figure 13: CAD model of the EM setup: top view

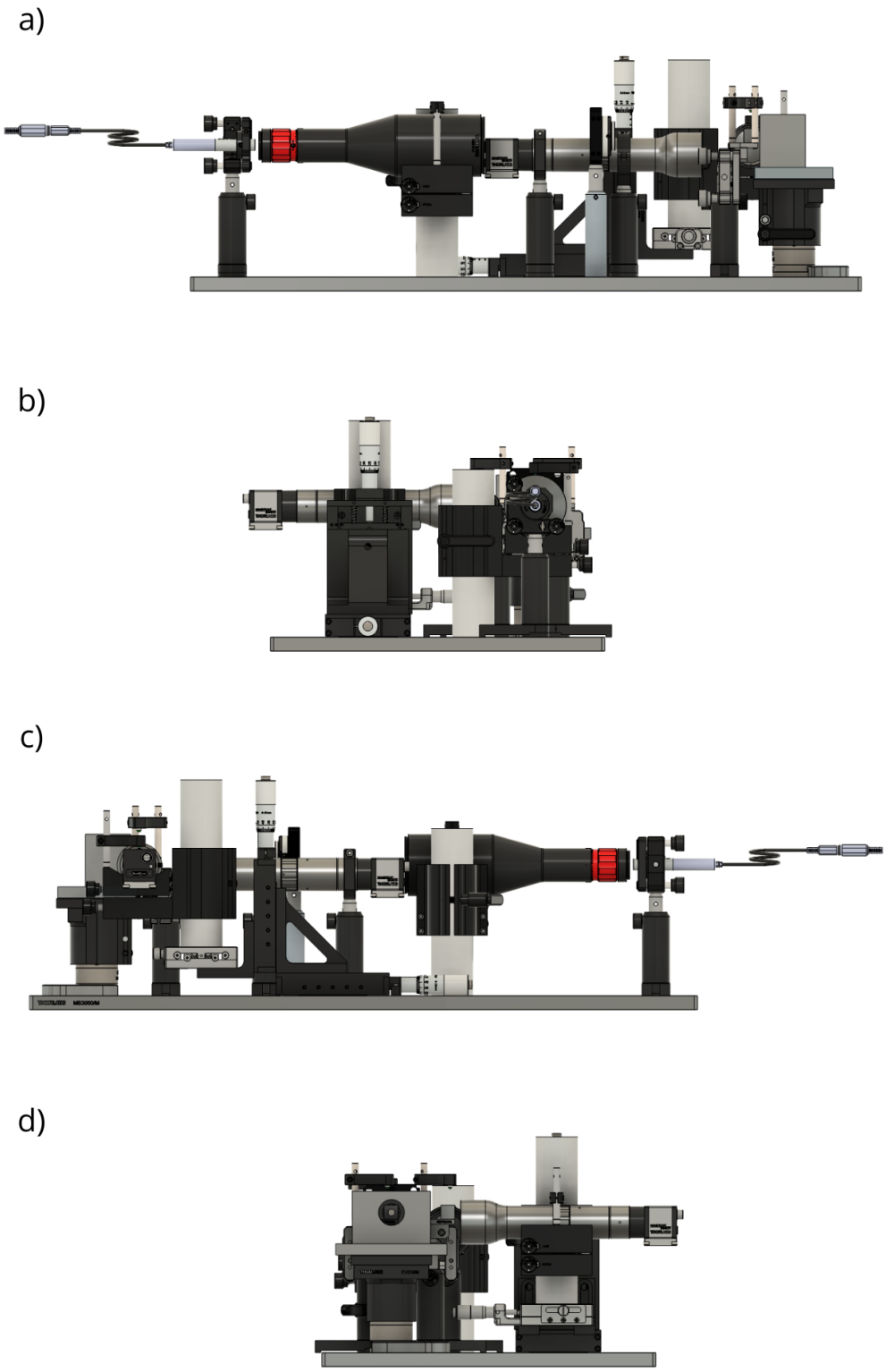

Figure 14: CAD model of the EM setup: *a)* right side view, *b)* front view, *c)* left side view, *d)* rear view

2.3 Numerical simulations and calculations

As the objective of the EM setup is to measure the WF aberrations, the specifications of the WFS's relay lens had to be found out so that the pupil plane within the EM would be imagined by the relay lens onto the microlens array of the WFS correctly. First of all, the minimal possible WD of this telecentric relay had to be determined. This was done, as already stated above (Section 2.2), using the CAD model. In this model, the absolute distance from the pupil plane to the edge of the second beam splitter was measured multiple times. The result had to be recalculated as the path of the inspected distance included both of the beam splitters. Thus the OPLs within the beam splitters had to be taken into account. The final result was rather approximate, however, provided an estimate of the real distance: 93 mm. This value implied that the WD of at least 100 mm would be needed for the telecentric lens. Second step was to determine a suitable telecentric lens by comparing the magnification (and thus the FOV for the given WFS) for the combination of the telecentric lens and the cornea's refraction. For this objective, simulations in ZEMAX OpticStudio were carried out. Three different telecentric lenses were tested in these simulations. Models of the lenses were provided by Edmund Optics Inc. as "black boxes". These were incorporated into the ZEMAX EM which was used in [39]. The EM was also adapted by leaving out the unnecessary parts meaning that only the cornea was kept in place. Thus the ZEMAX model for the simulations featured the cornea, the WD and the "black box" model of a particular telecentric lens. The WD was slightly adjusted for the best focus in each simulation and the values of the paraxial magnification (PMAG) were noted down. The comparison of the three tested telecentric lenses can be found in Table 2. Figure 15 illustrates the "black box" of one of the telecentric lenses, Figure 16 depicts the setup for the simulation.

Table 2: Comparison of three telecentric lenses theoretically eligible to be used as the relay lens of the WFS

Model	WD [mm]	Measured PMAG	FOV [mm]
#63074	120	-0,567	10,49 x 8,40
#56678	103	-0,680	8,75 x 7,00
#67731	100	-0,850	7,00 x 5,60

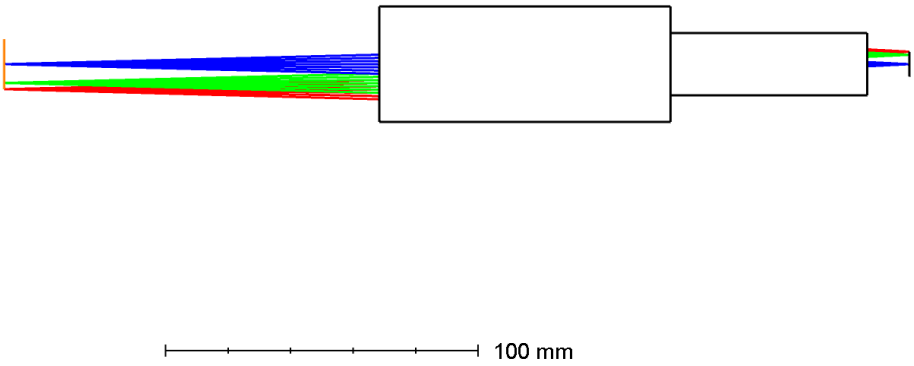

Figure 15: The "black box" telecentric lens ZEMAX model provided by Edmund Optics Inc.

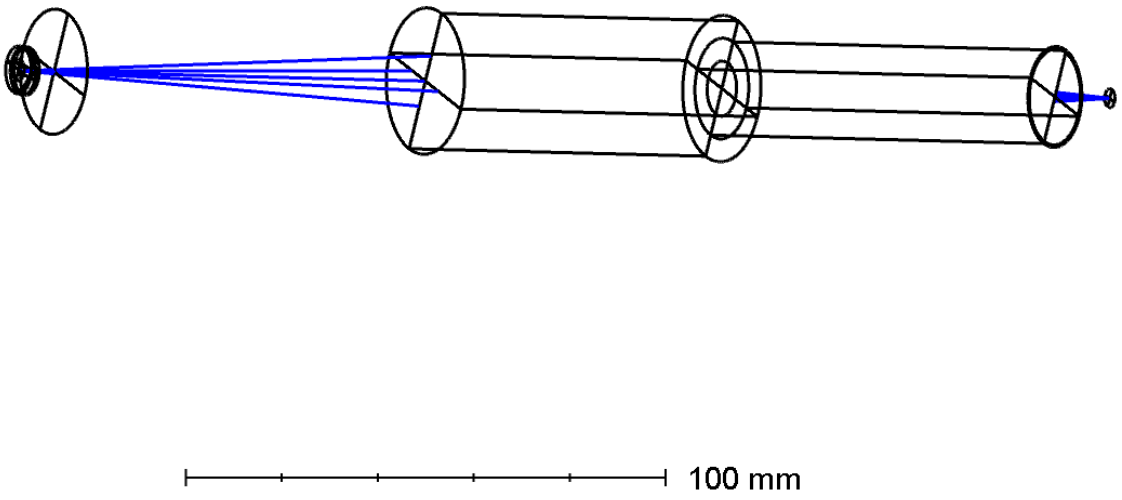

Figure 16: The ZEMAX model of the cornea and telecentric lens combination

Based on the results in Table 2, the #67-731 telecentric lens was chosen as the relay lens for the WFS having a feasible WD and providing the best magnification and reasonable FOV at the same time.

2.4 Artificial retina

The model of retina is needed within the new design of the EM to provide a "screen" on which the laser beam entering the EM can be focused thus creating a point source of light for the back illumination. The model has to feature ideal scattering properties while enabling for measurements in water environment. In [39], two approaches of modelling retina were mentioned – [3] [22]. The literature research done within this thesis could not reveal any better sources of inspiration. The method outlined in [22] is for the purpose of this thesis unnecessarily advanced, complex and not even of the same objective. However, 3D printing was considered worth trying.

First, three pieces of white PLA material were printed. These models were of a cylindrical shape, 3 mm thick and 13 mm in diameter. For the sake of simplicity, the radius of curvature of the human eye retina was not implemented to the model retina design. Each of these models was after the printing polished with a sandpaper. Circular movements along the paper were used to polish the models. During this procedure it was found out that the thickness could be insufficient and mainly that the filling parameter of the 3D printing was set badly not being 100 % which resulted in uncovering of the inner structure by the polishing process. This implied a new set had to be printed. The second print was set with the filling factor 100 %, white PLA was used again, the thickness was changed to 5 mm. The diameter was kept the same as it is determined by the dimensions of the retinal adapter of the EM. Four pieces were printed in total. Surface of each piece was first polished by a P150 sandpaper. One of the models was only polished by this paper, not by finer ones. Each of the remaining models was polished with a different sandpaper – P400, P800 and P1200. With this method, a set of four models with different surface roughness characterised by the specification of the sandpaper was created. For comparing the particular retinal models and selection of the best one, the auto-exposure value of the WFS acquired in the WFS Software was used. Each retina was placed into the EM and tested in the same conditions. This method, however, was not discriminate. The WFS did not respond to the changes of retina models with any change of its auto-exposure value. For this reason, in the end, the most smooth retina model, the one polished with P1200 sandpaper, was selected to be utilised. This choice was based on assumption that the surface roughness of this model is the closest one to the required scattering. The first unused set of the model retinas can be seen in Figure 17, Figure 18 illustrates the machining process.

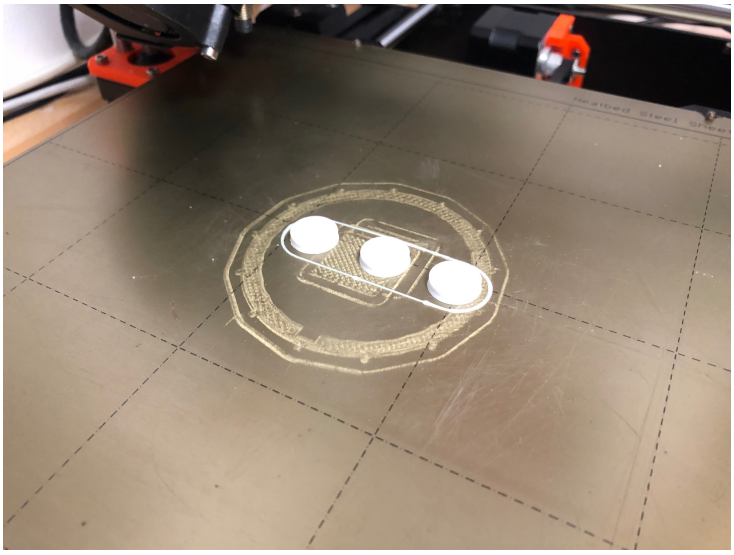

Figure 17: The first set of 3D printed PLA artificial retina models

Figure 18: The process of polishing the surfaces of the model retinas with sandpaper of different grain sizes

2.5 Assembly process of the new eye model setup

This section describes the actual assembly process of the new mechanical EM setup. The process progressed as follows although some less important steps might be omitted in the description. The whole EM setup was mounted onto a base plate screwed to an active vibration isolating optical table. The laser diode needed to be aligned first. The height-limiting factor, as the height of the laser beam above the optical table in optical setups is an important measure, was found to be the height of the BE. Thus the laser diode was set approximately to the lowest

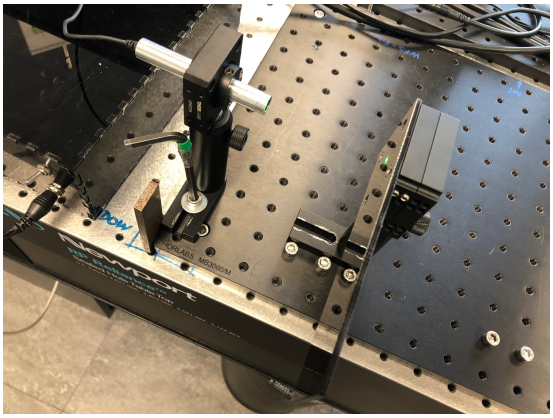

Figure 19: Laser alignment using a special aligning tool, part 1

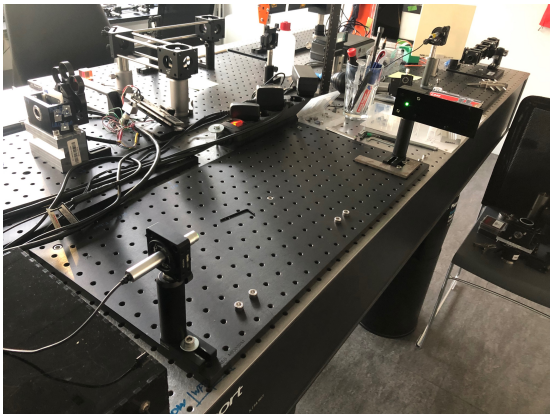

Figure 20: Laser alignment using a special aligning tool, part 2

possible height of the BE. A special aligning tool was used to achieve a parallel (with the optic table) path of the laser beam (See Figure 19 or 20). The EM on its stage was firstly adjusted for the laser beam height and then placed to the corner of the base plate and aligned with both its edges but yet not fixed in the position (except for its post). Although most of the components were mounted on posts with post bases thus not aligned with the screw holes, the edges of the base plate together with the screw holes where facilitating the whole process of the assembly. The EM served as a reference to reposition the laser closer to the edge of the base plate. Then, the EM was demounted and its aligning stage was used for the precise laser beam alignment. For this process, an optical mirror was used. After this procedure, an alignment check was performed with the use of the special aligning tool and a ruler (Thorlabs Inc.). The precision was assessed to be the highest achievable. Once the laser was perfectly aligned, the EM was placed back onto its post, aligned and fixed in its position.

The next step was perhaps the most complicated of the whole assembly – the alignment of the BE. The pitch of the BE's mount was adjusted approximately using a water level. Its height was set by an adjusting collar located on the post under the mount. The determination of the position for the post of the BE was facilitated by a large square tool/ruler and done by moving the post along this tool while simultaneously visually observing the alignment of the BE with the laser beam (See Figure 21). This way the post's position was found. The height was set again and the mount was locked in position that was determined by observing the mutual positions of the laser diode and the BE, and also the image produced by the BE on a white screen located near the EM. The fine tuning was carried out using the pitch and yaw knobs of the BE's mount and facilitated by watching the image on the white screen again. Later, the alignment was checked by a WFS and found to be sufficiently good.

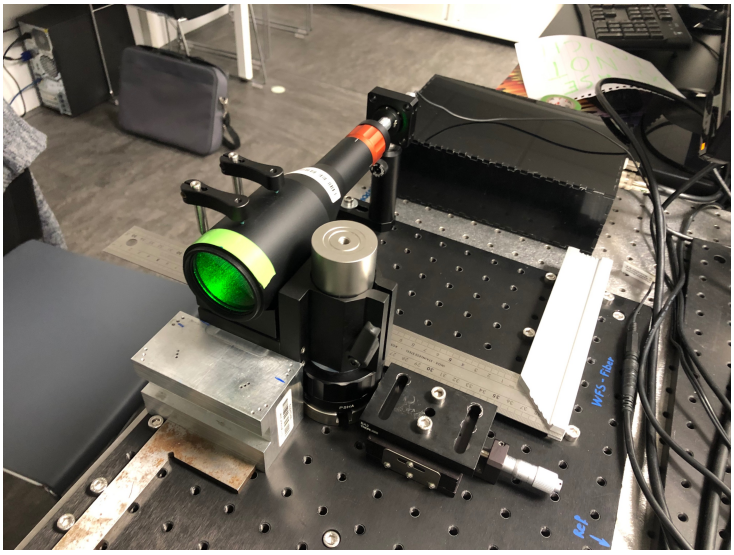

Figure 21: Determining the right position for the post of the BE

The iris diaphragm adjustment and alignment was not as hard as that of the BE. Its height was set with the help of the slide-in pupil modules placed into the EM. A square tool and the edge of the base plate were used to align the iris precisely with the EM. The beam splitters were manipulated onto their kinematic mounts using gloves. The height of the beam splitters' mounts was found using reflections of the aligned laser on the edges of the cubes. The first beam splitter was placed as close as possible to the EM to ensure sufficient WD. The beam splitter was aligned using the aligning tool and kinematic mount knobs. Second beam splitter was placed as close to the first one as possible, again for the sake of the WD, and was aligned using similar procedure. The alignment of the imaging camera together with its telecentric lens also took some time and was done by using the image of the IOL and its surrounds obtained from the camera. Point Grey Software was utilised for the image acquisition. Using the CAD model, the specific position on the base plate for the 3-axes stage of the WFS and its relay lens was found easily. After assembling the whole stage, the post with the mount for the 0,75x telecentric lens were placed onto the small translation stage and aligned visually with the light direction. Precise alignment would be possible by using the pitch and yaw knobs. An adapter had to be mounted between the WFS and the telecentric lens, as the lens' focal length did not correspond to the distance between the front housing and the optical reference plane of the WFS (location of the microlens array). Contrary to the imaging lens, in the end, it was not feasible to align nor focus the WFS properly. This issue is further discussed in the chapter 3 Results and Discussion.

2.5.1 Components used in the enhanced eye model setup

Laser diode

As the source of illumination, CPS532 (Thorlabs Inc.) dioded-pumped solid-sate laser was used. This laser source with compact dimensions provides a collimated elliptically-polarised round beam with diameter of 3,5 mm and wavelength equal to 532 nm. With 4,5 mW of power this laser diode falls under the 3R laser safety class. Thus direct eye exposure should be avoided. Considering the fact, that the setup is designed only for EM measurement *ex vivo*, this safety class is not problematic. [34]

Beam expander

To provide the necessary width of illuminating beam, GBE15-A (Thorlabs Inc.) Galilean BE was implemented into the setup. This component maintains the beam orientation, features AR (anti-reflective) coating within 400-650 nm with specified transmission 96 % at 543 nm and sliding lens adjustment to minimize the walk off of the beam. This BE expands the beam of maximal input diameter of 2,9 mm 15 times. Maximum input beam diameter for output PV WF error (diffraction-limited) $< \lambda/4$ at 633 nm is 2,5 mm for this particular component. [35]

Iris diaphragm

For the regulation of the amount of light within the system, SM1D12C (Thorlabs Inc.) ring actuated iris diaphragm was utilised. This diaphragm has the size of apertures adjustable within the range of 1-12 mm. The aperture size can be read out using a numerical scale on its circumference and may be fixed by a locking screw. [37]

Beam splitters

Two pieces of BS004 (Thorlabs Inc.) non-polarising cube beam splitters were used in this setup. With the edge of the cube measuring 1/2" (12,7 mm), these are big enough to transmit all the light coming from the EM further to the sensor devices. Beam splitters use beamsplitter coating for 400-700 nm, and AR coating on all input surfaces. The manufacturer claims the surface flatness and the WF error at 633 nm to be $\lambda/10$ and $< \lambda/4$, respectively. The ratio of reflectance to transmission is 50:50. Some of the light is getting absorbed within the AR coating. The use of economy visible beam splitters (such as EBS2, Thorlabs Inc.) was considered, however, these do not comply with the optical requirements due to the double reflection on the two surfaces that they have. [36]

Eye model

For the EM, the model presented in [39] was of course used, with one change only – the model retina, as already discussed in 2.4.

Telecentric lens for imaging

The imaging of the position of the IOL within the tilt-shift device of the EM within the measurement setup is provided by #63-074 (Edmund Optics Inc.) telecentric lens. This lens works at 120 mm WD, has a 0,5x magnification and features 425-675 nm BBAR coating. Its numerical aperture equals 0,041, FOV for the maximal sensor format (1/1,8") is 14,4 mm x 10,8 mm being more than sufficient for the position examination purpose. The aperture is adjustable within f/6-f/22 which was appreciated during the alignment process. [10]

Imaging camera

FL3-U3-13E4M-C (FLIR Systems, Inc.) monochromatic camera images the tilt-shift unit with the IOL to enable assessment of the correct alignment within the setup. The camera works with CMOS sensor format 1/1,8" (being the maximal sensor format for the telecentric lens described above). The resolution is 1,3 Mpx (1280 x 1024 pixels; one pixel having the size of 5,3 μm) with the sensing area of 6,78 x 5,43 mm. The camera features the frame rate of 60 FPS and exposure time within 16 μs-1 s. [11]

Telecentric lens for the wavefront detection

As the relay lens for the WFS, #67-731 (Edmund Optics Inc.) 0,75x telecentric lens is used. This component is a part of the same series as the imaging telecentric lens, thus having the same coating and adjustable range of f-numbers. Other parameters are different: the WD of 100 mm, magnification equal to 0,75x, numerical aperture 0,062, FOV (for the maximal sensor format (2/3")) 11,7 x 8,8 mm. This lens was chosen because it fulfills the requirements for this application as described in [39]. The lenslet array lies in the conjugated plane with the pupil plane, as it was simulated in 16, and the magnification was calculated so as the resulting image fits the sensor and at the same time enough local gradient measurement points are provided. (See 2) The rather long WD should be sufficient to prevent the mechanical interference of the telecentric lens with the EM, although, only approximately 7 mm were estimated as the manipulating distance for alignment. [10]

Hartmann-Shack wavefront sensor

The WFS utilised for this setup is WFS150-7AR Shack-Hartmann WFS (Thorlabs Inc.) combined with a microlens array MLA150-7AR (Thorlabs Inc.). The camera of the sensor incorporates a CCD sensor and has maximal resolution of 1280 x 1024 pixels (can be changed to lower resolution). The pixel size is 4,65 x 4,65 μm resulting in sensor size of 5,95 x 4,76 mm. The exposure ranges from 79 μs to 65 ms. The WF accuracy at 633 nm is $\lambda/15$ RMS. The distance from the front housing to the optical reference plane, where the microlens array is located, is 13 mm.

The WFS operating principle is based on using the local gradient of the WF on a number of bright spots generated on the sensor by the microlens array and from these gradients the WF can be reconstructed using the reference spots theoretically located on the OA of the microlenses. [38] [39]

Microlens array

The MLA150-7AR lenslet array accepts 400-900 nm light. Its effective focal length is 5,2 mm. The number of active lenslets is selectable within the software with maximum of 39 x 31 lenslets. The pitch of the lenslet is 150 μm. [38]

3 Results and Discussion

The current, and for this thesis final, status of the EM setup can be seen in Figures 22, 23, 24, and 25. With regards to these photographs, it can be seen that the EM was assembled completely (compare to the CAD model in 12). The photographs show the ultimate version after the whole alignment process described in Section 2.5. This setup, as it is, can now be used, however, only for imaging the IOL in the EM with the imaging camera. The alignment of the WFS could not be finished which is not directly obvious from the presented photographs. This issue was found to be caused by the properties of the model retina and is discussed in following sections.

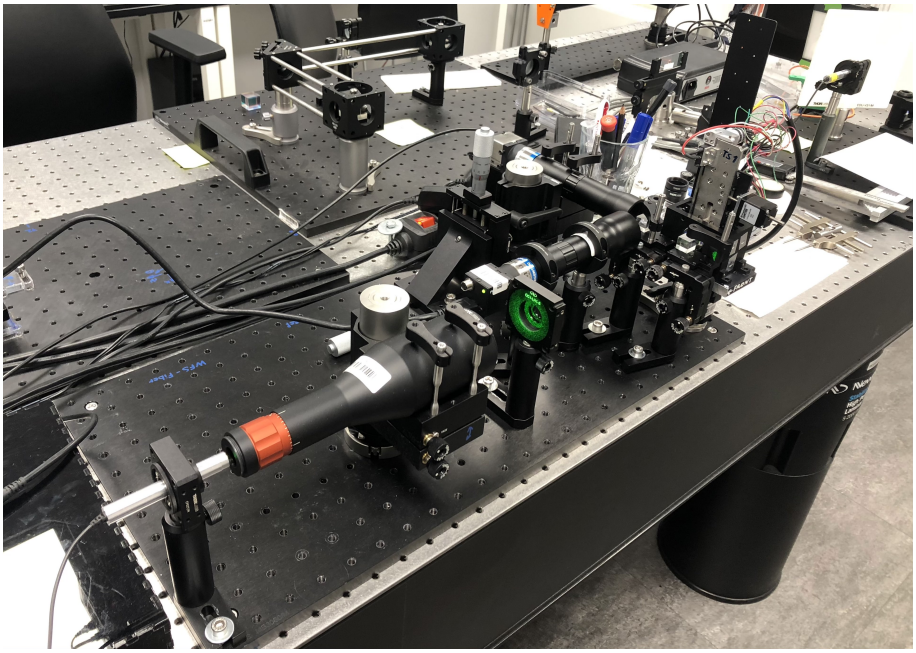

Figure 22: The assembled EM setup: general view

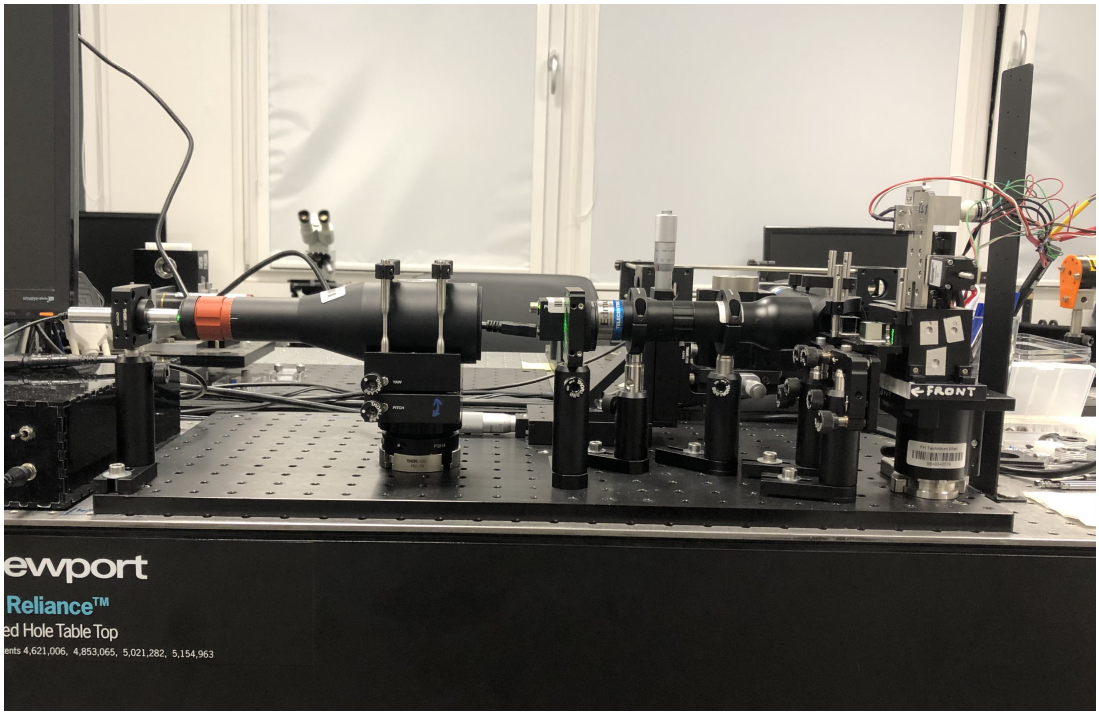

Figure 23: The assembled EM setup: side view

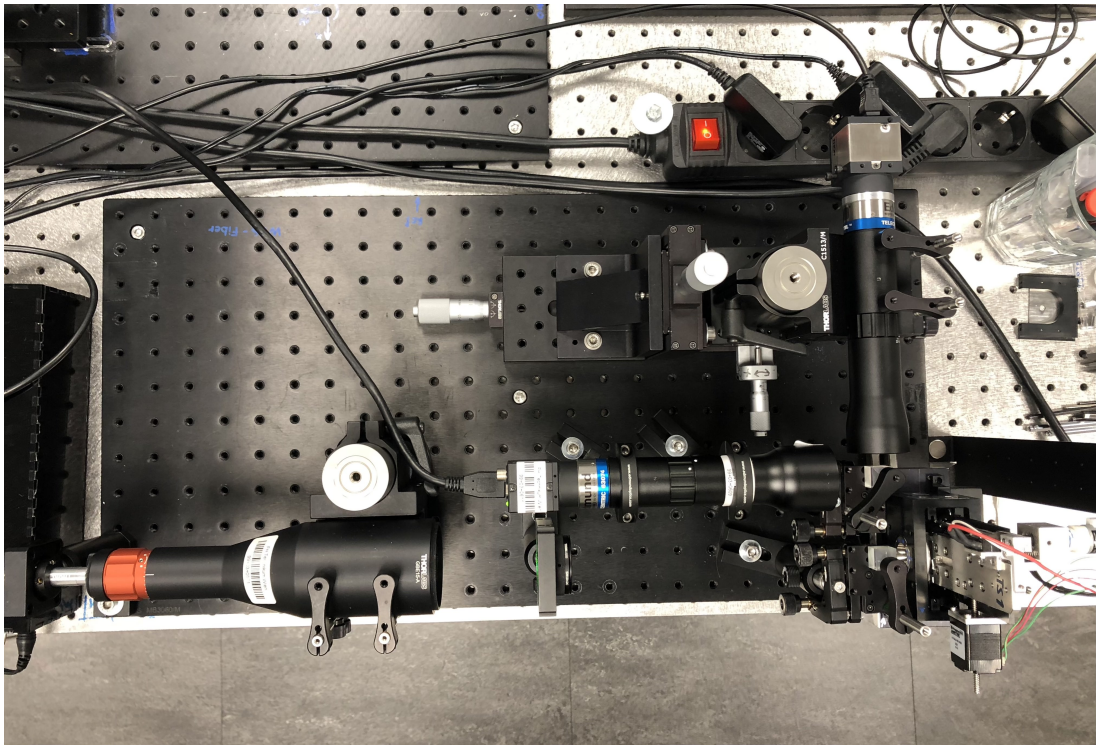

Figure 24: The assembled EM setup: top view

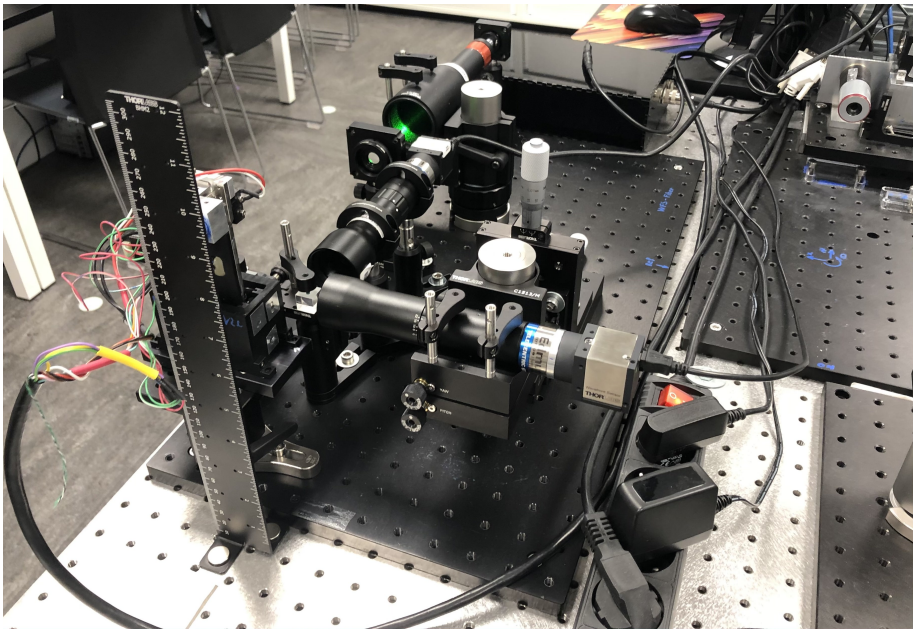

Figure 25: The assembled EM setup: opposite general view

The images of the IOL from the imaging camera are shown in Figure 26 and 27. The first image shows the IOL within the holder of the tilt-shift unit inside the EM. The second image depicts the same setup, only with a black plastic tweezers located behind the IOL, in front of the model retina.

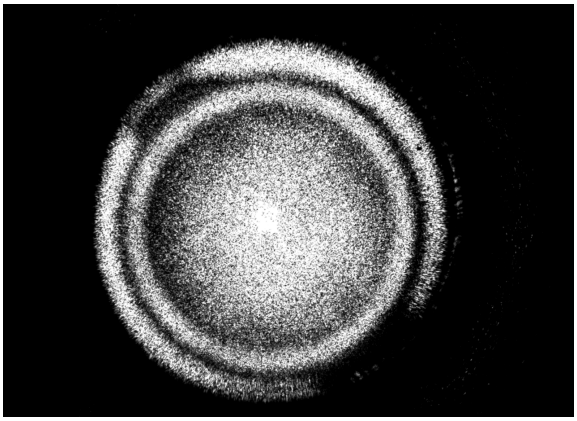

Figure 26: Image of the IOL within its holder inside the EM (acquired with the imaging camera)

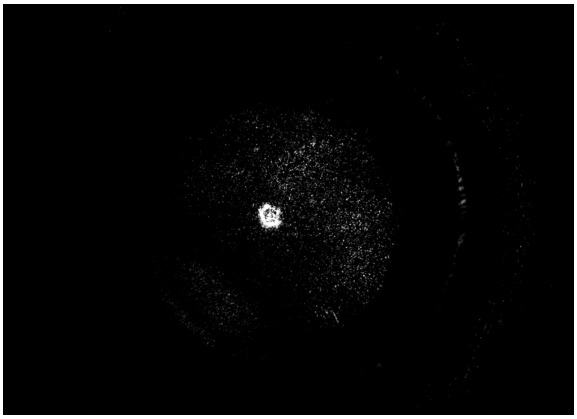

Figure 27: Camera image of the IOL with black plastic tweezers located behind the lens and blocking the light from the retina model so as to determine the source of illumination for the camera

Spotfield graph images from the WFS Software which were acquired during the process of determining the sufficiency of the scattering properties of the retina model are depicted in Figures 28, 29, 30. A spotfield graph shows the raw data image of the distribution of intensity of the light falling onto the WFS after being focused by the microlens array. Figure 28 shows

the spotfield graph acquired when no slide-in pupil module was present in the EM. Figure 29 features the spotfield graph recorded when the slide-in module with pupil of 4,5 mm was inserted into the EM. Figure 30 shows a difference of the previous two images with the aim of highlighting a circle of higher intensity potentially present in Figure 29.

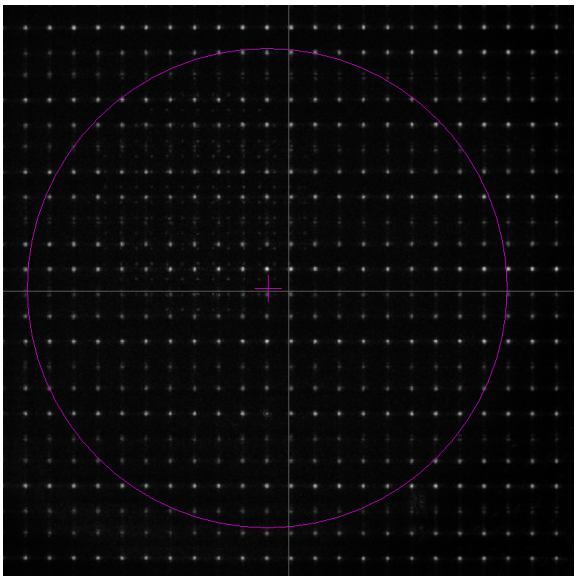

Figure 28: The spotfield graph while no slide-in pupil module was present in the EM

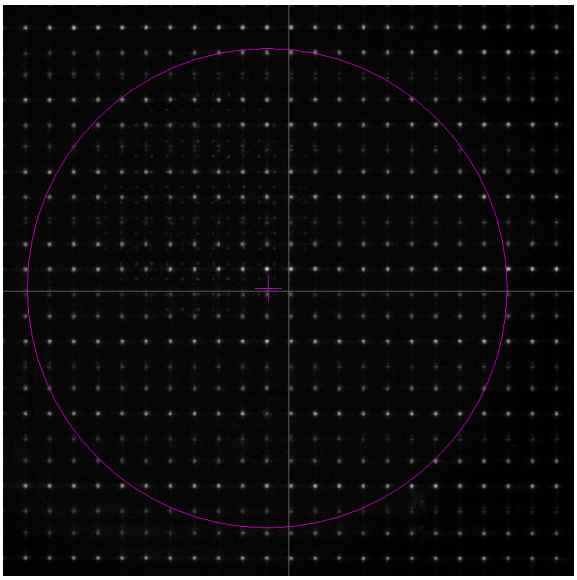

Figure 29: The spotfield graph while the slide-in pupil module was present in the EM

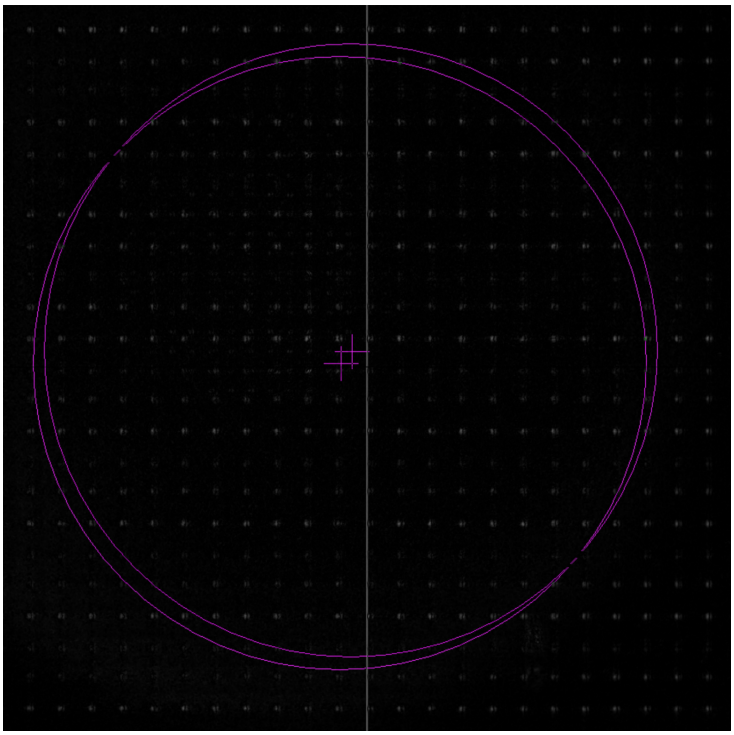

Figure 30: Subtraction of the two images featured in Figures 28, 29

3.1 Retina model as the limiting component

During the process of the WFS alignment it was discovered, that the amount of light coming from the back of the IOL is not sufficient for the intended purpose. This was deduced upon the fact that after inserting the pupil slide-in module into the EM, the observed image of the spotfield graph did not change in a significant way. Compare Figures 28 and 29. The change should be visible as a high intensity circle in the centre of the graph while the surrounding areas should be obscure when the pupil is present in the EM. This is not what happened. An attempt to identify this circle of higher illumination is depicted in Figure 30. This is a subtraction of the two previous images which should ideally result in a better visibility of the expected circle, which is not this case. Contrary to this, reducing the diameter of the iris diaphragm affects the image of the spotfield graph. This indicates that most of the light falling onto the WFS does not come from within the EM but from elsewhere. The amount of light coming from the backside of the IOL is, though, sufficient for the imaging camera, as can be seen in Figures 26 and 27. After placing tweezers behind the IOL, the image from the camera is lost (Figure 27). However, the change is not observable in the WFS measurement. The affect of the light reaching the WFS from outside the setup through the first beam splitter (from the direction perpendicular to a line connecting the laser diode and the EM) was found to be negligible. Knowing this, the only remaining option is that most of the light falling onto the WFS comes from reflections of the cornea and the IOL. This is a huge complication as the majority of the light has to come from behind the IOL to enable for accurate measurements because otherwise the measured WF is not a representation of the IOL properties.

The retina model, thus, is not providing enough scattering as it should. The cause of that is most likely in the polishing process. The sandpaper P1200 (average particle size 15,3 μm [30]) does not provide grains sufficiently small to induce the desired scattering. The particles ensuring the required scattering should be of the similar size as the used wavelength providing a diffusive reflection. [33] Similar properties as the human retina features should be provided by the model retina. The neural layer of retina with its thickness of 200 μm has the scattering coefficient μ_s equal to 20 mm^{-1}. The retinal epithelium scatters the light the most having μ_s of 170 mm^{-1}. [14] These parameters have to be taken into account.

If a functioning retina model is developed, then the alignment of the WFS, mediated by the 3-axes translation stage and pitch and yaw knobs of the telecentric lens mount, becomes feasible. The pupil slide-in module can be used for this purpose. As the magnification in the conjugate plane is known as well as the diameter of the pupil in the plate, its image size can be calculated. To align the WFS in the x-y plane, a circular image of the pupil has to be found and brought to the centre of the FOV. Fine tuning is done by the yaw and pitch knobs to secure as planar wave as possible. Later, while aligning the WFS in the z-axis, the image of the pupil with the calculated size has to be found in the spotfield graph of the WFS Software. The measurements then can be carried out using the WFS Software feature that enables choosing the region of interest (ROI; 3 and 4,5 mm in width to simulate the pupil).

3.2 Achieved improvements

The developed EM setup mimics the human eye better by using an artificial retina model. The setup is thus more realistic resembling methods and devices used in clinical ophthalmology where it potentially might be used in future. The "machine vision" setup was successfully implemented into the measurement setup. By using the feature of the WFS Software, the slide-in pupil modules can be omitted. The way the whole setup is constructed now prevents the geometrical aberrations that were induced by the retinal window in the previous setup.

3.3 Potential sources of error

Results cannot be really investigated here for the amount of error but still a few things can be mentioned as a possible causes of errors. Modest aligning technical possibilities and technique definitely belong amongst these. By that e.g. using a tape to attach mirrors to a stage for the laser alignment, too many degrees of freedom of the mounting stages, or using screwing holes of the base plate together with the heads of the screws as reference, can be understood. Regarding the finished EM setup, the possible error causing feature are the rods of the beam splitter mounts because of the light reflections on them. Another issue is the light coming to both telecentric relays from the unused faces of the beam splitters.

3.4 Suggestions for future improvements

Once a well-functioning retina model is developed and implemented, there will still remain some space for improvement. Furthermore, other imperfections may occur during that process. A second light source could possibly be used instead of the BE. This light source would provide illumination for the imaging camera. Different wavelength should be used to avoid interference with the light for measuring. As its alignment is rather complicated, leaving out the BE can help to reduce the amount of aberrations created by the OS outside the EM. The iris diaphragm, which was formerly thought to be necessary to simulate for the photopic and scotopic illumination, can also be omitted then. Another potential source of noise would be eliminated this way. Implementing shades into the setup on various positions could also help in reducing the amount of the noise and add to the accuracy of the final results.

4 Conclusion

The aim of the present paper was the enhancement of an existing optomechanical EM. Incorporating the "machine vision" and bringing more physiology by introducing an artificial retina model into the whole setup was the main objective. A new setup with improved layout was designed. Later, a CAD model of this design was developed and finely tuned. Measurements and calculations were carried out based either on the CAD model, or the ZEMAX OpticStudio simulations. After determining all necessary components, the EM setup was assembled. Although a new model of retina has to be developed to finish the EM setup and enable performing of the real measurements, the achieved outcome seems promising in ability of reaching this goal. Excluding the necessary replacement of the model retina, there is still some space for improvement in the present setup. Major changes can be done by incorporating a second light source and thus omitting the use of the BE and the iris diaphragm.

Bibliography

[1] M. S. de Almeida and L. A. Carvalho, "Different schematic eyes and their accuracy to the in vivo eye: A quantitative comparison study," *Brazilian Journal of Physics*, vol. 37, pp. 378–387, 2007. DOI: 10.1590/S0103-97332007000300008.

[2] M. Bass, *Handbook of Optics, Volume III: Vision and Vision Optics*, 3rd ed. USA: The McGraw-Hill Companies, Inc., 2010, ISBN: 978-0-07-162928-7.

[3] S. Bonaque, P. Bernal, M. Marcos-Robles, and N. López-Gil, "Optical characterization method for tilted or decentered intraocular lenses," *Optometry and vision science : official publication of the American Academy of Optometry*, vol. 93, Apr. 2016. DOI: 10.1097/OPX.0000000000000851.

[4] J. D. Cameron and D. M. Rašić, "The crystalline lens," in *Eye Pathology: An Illustrated Guide*, S. Heegaard and H. Grossniklaus, Eds. Berlin, Heidelberg: Springer Berlin Heidelberg, 2015, pp. 173–195, ISBN: 978-3-662-43382-9. DOI: 10.1007/978-3-662-43382-9_5. [Online]. Available: https://doi.org/10.1007/978-3-662-43382-9_5.

[5] S. Čanović, S. Konjevoda, A. Pavičić, and R. Stanić, "Intraocular lens (iol) materials," in Nov. 2019, ISBN: 978-1-83880-484-8. DOI: 10.5772/intechopen.89985.

[6] L. Carvalho, "Accuracy of zernike polynomials in characterizing optical aberrations and the corneal surface of the eye," *Investigative ophthalmology & visual science*, vol. 46, pp. 1915–26, Jul. 2005. DOI: 10.1167/iovs.04-1222.

[7] S. Čech and D. Horký, *Histologie a mikroskopická anatomie pro bakaláře*, 2nd, rev. ed. Brno: Masarykova univerzita, 2011, ISBN: 978-80-210-5544-5.

[8] S. Dewey, M. Colvard, L. B. Arbisser, S. L. Jick, and D. V. Gangadhar, "Focal points: Clinical modules for ophthalmologists," vol. 33, no. 8, 2015, ISSN: 0891-8260.

[9] R. C. Eagle, *Eye pathology, an atlas and text*, 3rd ed. Philadelphia: Wolters Kluwer, 2017, ISBN: 978-1-4963-3717-7.

[10] Edmund Optics Inc., *Silvertl™ telecentric lenses*, Barrington, NJ, USA, 2022. [Online]. Available: https://www.edmundoptics.com/f/silver-telecentric-lenses/12802/.

[11] Edmund Optics Inc., *Usb cameras*, Barrington, NJ, USA, 2022. [Online]. Available: https://www.edmundoptics.eu/c/usb-cameras/1013/.

[12] Eurostat, *Health in the european union – facts and figures*, 2020. [Online]. Available: https://ec.europa.eu/eurostat/statistics-explained/index.php?title=Health_in_the_European_Union_%E2%80%93_facts_and_figures (visited on 03/09/2022).

[13] Eurostat, *Eurostat regional yearbook, 2021 ed.* Luxembourg: Publications Office of the European Union, 2021, ISBN: 978-92-76-37761-0.

[14] A. Gerakis, M. Kirillin, E. Sergeeva, M. Makropoulou, and A. Serafetinides, "Monte carlo modeling of corneal and retinal optical coherence tomography imaging," in *2008 8th IEEE International Conference on BioInformatics and BioEngineering*, 2008, pp. 1–6. DOI: 10.1109/BIBE.2008.4696840.

[15] C. Gerhard, *Lens Design Basics*, ser. 2053-2563. IOP Publishing, 2020, ISBN: 978-0-7503-2240-9. DOI: 10.1088/978-0-7503-2240-9. [Online]. Available: https://dx.doi.org/10.1088/978-0-7503-2240-9.

[16] C. Holló, K. Miháltz, M. Kurucz, *et al.*, "Objective quantification and spatial mapping of cataract with a shack-hartmann wavefront sensor," *Scientific Reports*, vol. 10, Jul. 2020. DOI: 10.1038/s41598-020-69321-3.

[17] International Centre for Eye Health, "Cataract surgical rates," *Community Eye Health Journal*, vol. 30, no. 100, pp. 88–89, 2017, ISSN: 0953-6833. [Online]. Available: https://pubmed.ncbi.nlm.nih.gov/29483754.

[18] International Organization for Standardization, *International standard iso 11979–2:2014, Ophthalmic implants – intraocular lenses – part 2: Optical properties and test methods*, 2014 ed., Switzerland, 2014.

[19] F. Kretz, S. Scholtz, and G. Auffarth, *A brief history of iol materials*, United Kingdom, 2014. [Online]. Available: https://theophthalmologist.com/subspecialties/a-brief-history-of-iol-materials.

[20] G. K. Lang and O. Gareis, *Opthalmology, a pocket textbook atlas*, 2nd, rev. ed. Stuttgart: Thieme, 2007, ISBN: 978-3131261625.

[21] M. W. Leitman, *Manual for eye examination and diagnosis*, 9th ed. Hoboken: Wiley Blackwell, 2017, ISBN: 978-1-119-24361-8.

[22] B. Lorber, W.-K. Hsiao, and K. Martin, "Three-dimensional printing of the retina," *Current opinion in ophthalmology*, vol. 27, pp. 262–267, May 2016. DOI: 10.1097/ICU.0000000000000252.

[23] V. N. Mahajan, *Aberration theory made simple*, 2nd edition. Bellingham: SPIE Optical Engineering Press, 1991, ISBN: 978-0-8194-8825-1.

[24] G. Markowsky. "Information theory." (2017), [Online]. Available: https://www.britannica.com/science/information-theory (visited on 03/09/2022).

[25] V. Mornstein, *Lékařská fyzika a biofyzika*. Brno: Masarykova univerzita, 2018, ISBN: 978-80-210-8984-6.

[26] O. Naňka, M. Elišková, and O. Eliška, *Přehled anatomie*, 2nd, rev. ed. Prague: Galén, 2009, ISBN: 978-80-7262-612-0.

[27] L. A. Remington, *Clinical Anatomy of the Visual System*, 2nd ed. Missouri: Elsevier, 2005, ISBN: 9780750674904. DOI: 10.1016/B978-0-7506-7490-4.X5001-7.

[28] R. Rokyta, *Fyziologie*, 3rd, rev. ed. Prague: Galén, 2016, ISBN: 978-80-7492-238-1.

[29] P. Rozsíval, *Oční lékařství*, 2nd, rev. ed. Prague: Galén, 2017, ISBN: 978-80-7492-316-6.

[30] *Sandpaper*, San Francisco, CA, USA, 2001. [Online]. Available: https://en.wikipedia.org/wiki/Sandpaper%5C#Grit_sizes.

[31] J. Sasián, *Introduction to aberrations in optical imaging systems*. United Kingdom: Cambridge University Press, 2013, ISBN: 978-1-107-00633-1.

[32] W. J. Smith, *Modern Optical Engineering*, 3rd ed. New York: McGraw-Hill, 2000, ISBN: isbn0-07-136360-2.

[33] H. Sun, *Lens Design: A Practical Guide*, ser. Optical Sciences and Applications of Light. CRC Press, 2016, ISBN: 978-1351722247. [Online]. Available: https://books.google.cz/books?id=uJO%5C_DQAAQBAJ.

[34] Thorlabs Inc., *Compact laser modules with phono jack*, 2022. [Online]. Available: https://www.thorlabs.com/newgrouppage9.cfm?objectgroup_id=1487%5C&pn=CPS532.

[35] Thorlabs Inc., *Fixed magnification beam expanders: Achromatic*, 2022. [Online]. Available: https://www.thorlabs.com/newgrouppage9.cfm?objectgroup_id=1580&pn=GBE15-A.

[36] Thorlabs Inc., *Non-polarizing cube beamsplitters (400 - 700 nm)*, 2022. [Online]. Available: https://www.thorlabs.com/newgrouppage9.cfm?objectgroup_id=754&pn=BS004.

[37] Thorlabs Inc., *Ring-actuated, sm-threaded iris diaphragms*, 2022. [Online]. Available: https://www.thorlabs.com/newgrouppage9.cfm?objectgroup_id=1479&pn=SM1D12C.

[38] Thorlabs Inc., *Shack-hartmann wavefront sensors*, 2022. [Online]. Available: https://www.thorlabs.com/newgrouppage9.cfm?objectgroup_id=5287.

[39] L. Traxler, "Testing the optical quality of intraocular lenses regarding postoperative tilt and decentration," doctoralthesis, Fachhochschule Technikum Wien, 2018.

[40] L. Traxler, N. Bayer, B. Reutterer, and A. Drauschke, "Improvement of optics, mechanics and the usability of a mechanical eye model for vision quality evaluation of iols," *IFAC-PapersOnLine*, vol. 48, no. 4, pp. 1–18, 2015, 13th IFAC and IEEE Conference on Programmable Devices and Embedded Systems, ISSN: 2405-8963. DOI: https://doi.org/10.1016/j.ifacol.2015.07.001. [Online]. Available: https://www.sciencedirect.com/science/article/pii/S2405896315007764.

List of Figures

List of Tables

List of abbreviations

BE beam expander

EM eye model

FOV field of view

IOL intraocular lens

MTF modulation transfer function

OA optical axis

OPL optical path length

OS optical system

PMMA polymethyl methacrylate

WD working distance

WF wavefront

WFS wavefront sensor